SCINTILLATING FIBER ARRAYS FOR IN-VIVO REAL-TIME PATIENT QUALITY ASSURANCE OF MEDICAL LINEAR ACCELERATORS

A Dissertation

presented to

the Faculty of the Graduate School

at the University of Missouri-Columbia

In Partial Fulfillment

of the Requirements for the Degree

Doctor of Philosophy

---

by

TYLER B. KNEWTSON

Dr. Enrique W. Izaguirre and Dr. Sudarshan K. Loyalka,

Dissertation Supervisors

December 2017

APPROVAL PAGE

The undersigned, appointed by the dean of the Graduate School, have examined the dissertation entitled

SCINTILLATING FIBER ARRAYS FOR IN-VIVO REAL-TIME PATIENT QUALITY ASSURANCE OF MEDICAL LINEAR ACCELERATORS

presented by Tyler B. Knewtson,

a candidate for the degree of doctor of philosophy,

and hereby certify that, in their opinion, it is worthy of acceptance.

Dr. Enrique Izaguirre

Dr. Sudarshan Loyalka

Dr. Lixin Ma

Dr. Tushar Ghosh

Dr. Mark Prelas

Dr. Robert Tompson

ACKNOWLEDGEMENTS

The work presented in this document has been completed over a period of intense learning and I would not have succeeded without the support of my professors, advisors, friends, and family. Thank you to everyone at the Nuclear Science and Engineering Institute, Baylor Scott and White Health, University of Tennessee Health Science Center, Methodist Le Bonheur Healthcare, and West Cancer Center for providing the resources to support my work. It has been a difficult but rewarding journey for me. Thank you, Dr. Ghosh, for sparking my interest in the medical physics program at the University of Missouri and Dr. Loyalka for guiding me along the way. Thank you, Latricia Vaughn, for all your help and support along the way. Thank you Dr. Izaguirre for helping me not only with my research but also for pushing me get involved in many advanced areas of medical physics and for helping me build the beginning of my career as a medical physicist. Thank you Sagar Pokhrel and Andy Wiles for your help solving difficult problems. I also want to thank my parents, Kelly and Dana Knewtson, for their support and guidance to help me reach my goals.

TABLE OF CONTENTS

LIST OF FIGURES

LIST OF TABLES

LIST OF EQUATIONS

SCINTILLATING FIBER ARRAYS FOR IN-VIVO REAL-TIME PATIENT QUALITY ASSURANCE OF MEDICAL LINEAR ACCELERATORS

Tyler Knewtson

Dr. Enrique Izaguirre and Dr. Sudarshan Loyalka, Dissertation Supervisors

ABSTRACT

The purpose of this research is to design real-time, in-vivo, transmission scintillating fiber detectors capable of identifying errors in external beam radiation therapy when a fraction of a treatment has been delivered. Two Cherenkov radiation corrected scintillating fiber detectors were constructed. These transmission detectors are fastened directly to the linac collimator using the accessory tray mount. One detector was developed for IMRT and consists of a linear array of 60 1.5mm square scintillating fibers aligned to the linac MLC leaf pairs. The second has higher resolution and is designed for SBRT/SRS. This real-time dosimeter is composed of two high-density orthogonal arrays of 128 0.5mm square fibers with a 0.8mm pitch and can capture angular projections to reconstruct 2D beam fluence with sub-millimetric resolution. The fibers are coupled to high-speed, high-gain optoelectronics and a high-speed analog-to-digital converter to process the output from each detector in real-time. The data is analyzed using in-house developed software to reconstruct the delivered dose and beam fluence. These novel detectors set a new benchmark for treatment accuracy and patient safety for radiation therapy treatments.

I. INTRODUCTION

Treating patients with a higher level of safety and accuracy is a continuing goal in the field of radiation oncology. As new technologies emerge, there are better ways to deliver radiation treatments to patients. However, as new technologies develop there can also be more complications. Nowadays, radiation therapy treatments can be quite complex and rely on many mechanical, electronic, and software components. It has become standard to perform quality assurance routinely on the machines so that it can be reasonably assumed that the treatments will go as planned. However, mechanical components, electrical components, and software could fail. The only way to be absolutely sure the patient is being treated as planned is to monitor the treatment in real-time. There are several types of detector systems in development with that goal in mind but they come with some serious limitations.

Transmission detectors based on large aspect ratio ion chambers and diodes are available today and are capable of detecting linac output such as a one-dimensional system using a tilted parallel ion chamber developed by iRT, an array of micro ion chambers developed by IBA, and a diode array developed by ScandiDos.[1-3] However, the ion chamber based systems require a high voltage polarization of the ion chambers' electrodes to operate, the sensitivity of these

types of detectors is limited and their operation can be complicated. Typically, the sensitivity of ion chambers is low because of the low efficiency of ion generation and collection. Additionally, ion chambers are an integrating type detector with a time constant on the order of several seconds. This makes them less than ideal for monitoring patient treatments in real-time on medical linear accelerators. Other technologies that are capable of operating at higher sensitivity than ion chambers, such as diodes, are not currently available for real-time treatment delivery detection. Presented in this dissertation is the first novel transmission detector design and implementation capable of monitoring patient treatments in real-time with high spatial and temporal resolution.

A. Scintillating fiber detectors

Polymer scintillating fibers consist of an optically clear polymer substrate that is doped with a scintillating organic dye that will emit visible light when a scintillating center is activated by electromagnetic radiation absorbed in the material.[4,5] The detection range can be from ultra-violet to high energy gamma photons and medium to high energy charged particles. The emission efficiency is determined by the scintillating material which is typically in very low concentration to avoid fluorescence self-absorption.[6] The low concentration of the scintillating material allows the optical absorption properties of the scintillating fibers to be defined by the properties of the substrate. Therefore,

the scintillating fibers have high optical transmission in the visible region of the electromagnetic spectrum and a water equivalent attenuation coefficient in the range of clinical x-ray, gamma, and electron energies.[6] These properties allow simplified dose measurements, making scintillating fibers an excellent material for clinical dosimetry.[7-9] Single point plastic scintillating dosimeters have been constructed by several authors and percentage depth dose (%PDD) data has been compared against ionization chambers and diode dosimeters using photon beams from 6 to 25 MV and electron beams from 6 to 21 MeV. For this range of energies, photon and electron beam dosimetry accuracy is within 1% respect to measurements performed with ion chambers.[7-9] These measurements validate the use of scintillating fiber detectors for clinical dosimetry and quality assurance. Scintillating fibers are energy independent for energies above 0.5 MeV and have excellent reproducibility, stability, and linear response in the range of clinical relevant doses (0.5 to 20 Gy).[7-9] Scintillating fiber arrays can be constructed using small cross section fibers (0.25 x0.25 mm^2) which can be utilized to construct detectors with a higher spatial resolution than ionization chambers or diode arrays.[7] For clinical electron dosimetry, they show less energy depth dependence than diodes because of the absence of the polarization effect.[10] Additionally, scintillating fibers do not require high voltage polarization, are water impermeable, and can be considerably thin with a practical limit of 100 um. Scintillating fibers suffer an annealing process when irradiated, which consists of a small

reduction of the fiber output of no more than 3% when the fiber is exposed to a cumulative dose of 10,000 Gy. In recent years, new scintillating radiation hard fibers have been developed which reduce the effect of radiation damage.[11] An example of these new fibers is our proprietary radiation hard scintillator fiber formulation used in the development of the detector presented in this publication.

B. Cherenkov radiation

The generation of Cherenkov radiation is a concern when using scintillating technology in the clinical energy range. Cherenkov radiation is a source of noise mixed with the scintillating signal proportional to the measured dose originated at the activated scintillator centers.[9,12,13] There are three proposed methods to subtract the Cherenkov radiation from the detector output. 1) Multi-channel discrimination which consists of an additional non-doped fiber that will produce only Cherenkov radiation. The Cherenkov radiation is then subtracted from the signal coming from the scintillating material to quantify only the scintillating emission,[9] 2) Time discrimination, which separates fluorescence from Cherenkov radiation using the time delay between fluorescence and Cherenkov emission; and 3) Spectral discrimination, which utilizes optical filters to separate the blue light (Cherenkov's emission) from the green light (fluorescence) emitted from the scintillating centers. Spectral

discrimination based on band pass filters to stop the Cherenkov radiation from reaching the detector has been successfully tested for single point dosimeters.[9]

In addition to filtering the Cherenkov radiation from the total scintillating fiber output, it is important to consider how the geometry of the detector design will affect the amount of Cherenkov reaching the end of the fiber where it is detected. For a transmission detector where the radiation field is normal to the scintillating fibers the amount of Cherenkov radiation detected will be less than 1.4% when using square scintillating fibers and clinical photon energies.[14] Utilizing a combination of the detector geometry and spectral filtering we eliminate the Cherenkov component of the signal to a null practical value.

C. Photodetection

Some fiber based detectors use bulky, fragile, and costly glass photomultipliers.[15] An alternative solution is to couple the fiber output to a CCD camera with a high number of channels. However, in this case, the detector is an integrating sensor and it cannot resolve the pulse nature of a linac beam output in real time.[16] Also, in a CCD based detector fiber arrays are coupled with non-scintillating fibers to transfer the scintillator output to the CCD camera sensor.[7,8] In addition, data transfer is not in synchronization with the linac pulse train which hinders the accuracy in the determination of the delivered dose. In conclusion, current technologies are unable to prevent

the mistreatments of patients or flag treatment deviations in the early stages of a treatment delivery and in real-time.

D. The real-time IMRT detector

To overcome the limitations of current devices, one solution is constructing a scintillating fiber detector capable of real-time treatment monitoring the can operate in transmission mode *in-vivo* during a patient treatment. The detector should be able to monitor a treatment and detect when the treatment is deviating from the intended delivery by estimating the total beam output when only a small fraction of the total treatment dose has been delivered. The detector utilizes novel architecture for high-speed and parallel signal detection, parallel synchronized analog-to-digital conversion, integrated signal processing, and analysis. This design is based on the use of scintillating fibers that are coupled directly to a monolithic detector with an embedded Cherenkov spectral discrimination filter, high-speed and high-gain front-end amplifiers and analog signal converters to achieve high throughput and real-time analog-to-digital conversion of the detector output. Using this system, it will be possible to overcome the limits of ionization chambers and diode based radiation detectors.

E. Hypo-fractionated treatment QA

The devices mentioned in the previous sections were specially designed for MLC technology used for typical IMRT treatments with leaf widths of 5mm or larger. However, newer technologies have been developed utilizing new high-resolution micro-MLC's for linacs such as the Brainlab Novalis system with a leaf thicknesses as small as 2.5mm and the Elekta Apex system with a leaf thickness of 2.5mm.

Considering the high doses involved in SRS and SBRT treatments and the use of high dose rate flattening filter free (FFF) linacs, there needs to be a real-time detector with the capability of monitoring small, high-resolution treatments in addition to monitoring standard IMRT treatments. Furthermore, SBRT and SRS treatments are designed to deliver high doses to a small volume with high gradients which makes the determination of the spatial modulation of the beam profile during treatments a requisite to prevent dose distribution errors that can affect the target dose and produce radiation complications to nearby organs at risk.

The temporal and spatial detection resolution characteristics of these detectors should be higher than the typical spatiotemporal modulation time and resolution of the linacs in SBRT and SRS treatments. Spatial resolution requirements in the direction orthogonal to the MLC is defined by the effective

thickness of the leaf pair beamlets at the plane of the detection which is smaller by a factor of 0.7 of the nominal MLC thickness defined at the linac CAX. Therefore, it is required that fiber array detectors should have higher resolution than the specified MLC thickness. In the direction parallel to the MLC, the spatial resolution should be higher than the expected modulation of the beam capabilities of the MLC encoders which is typically 1mm.

F. The SRS/SBRT detector

We present the development, characterization, and commissioning of the first *in-vivo,* transmission, high-resolution, real-time detector with the capability of reconstructing the 2D dose profile and the capability of detecting error departures when only a fraction of the beam is delivered with a temporal and spatial resolution that will limit errors to 2% of the treatment dose. The 3D reconstruction of the beam is achieved by acquiring multiple projections using a rotation system to determine the beam profiles in real-time. One of the remarkable features of the detector is the ability to provide live feedback to therapists or in automatic mode interrupt the linac to halt treatment if deviations in the expected dose occur during beam delivery. Finally, the detector is developed with electronics that are capable of achieving the detection of high dose rates without distortions originated by saturation or pulse pile up, and consequently, they can be used in the FFF SRS treatments.

II. THE REAL-TIME IMRT SCINTILLATING FIBER DETECTOR

A. Detector architecture overview

The main components of the detector include 1) an array of parallel arranged scintillating fibers, 2) a monolithic array of high speed, high gain Cherenkov corrected photodiodes, 3) a data acquisition system with parallel and synchronized analog-to-digital conversion, and 4) a local memory and data processing unit interfaced to a dedicated computer through a high speed optical link.

B. Fiber scintillator array

The scintillating fiber array is composed of 60 fibers that are aligned to match each of the Varian Millennium multileaf collimator's (MLC) 60 leaf pairs in a parallel mechanical and data generation architecture. Using this arrangement, each fiber can detect its respective beam segment as it is modulated by the MLC leaf pair. Each fiber has a 1.5x1.5 mm^2 cross section and the length is slightly longer than the maximum field size of medical linacs to ensure full beam profile sampling. The photodiodes and front-end electronics reside outside of the beam path but close enough to avoid additional Cherenkov radiation or noise from scattered photons. The fibers are embedded in a water

equivalent polymer support milled to provide a snug fit for each fiber to provide homogenous beam attenuation and minimal scattering while still providing rigid support for the fiber sensors. The estimated attenuation of the complete array including the fibers and the supporting material was measured to be 2.65% and scattering to be less than 1%. Fibers are coated with a black polymer film to seal them from ambient light. Figure 1 shows the layout of the fiber array and the detector mounted to the accessory tray of a Varian Clinac.

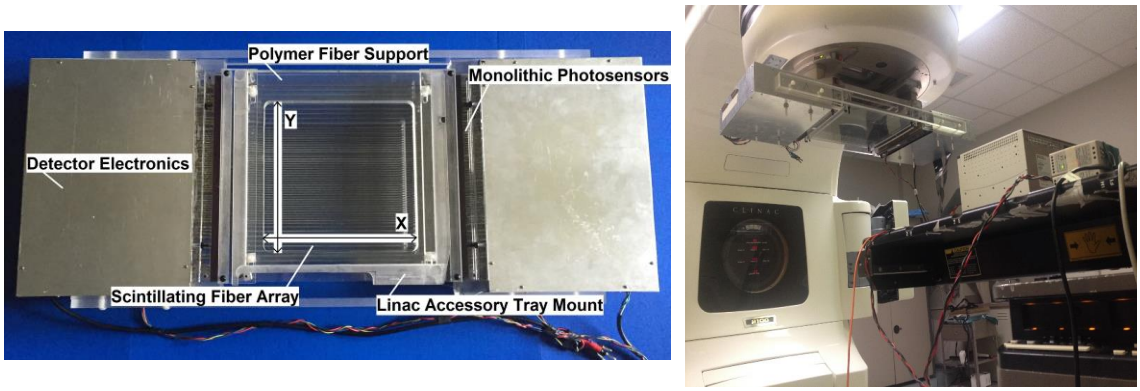

Figure 1. ***Detector System.*** At the left, a top view (from linac head to patient table) of the detector showing its main components. The x-axis corresponds to MLC leaf motion in the transverse direction and the y-axis corresponds to the longitudinal direction. At the right, the detector mounted on a Varian Clinac. The detector is aligned with respect to the MLC beamlets with a precision of 0.5 mm respect to the fiber and leaf centers.

Each fiber output is read using an in-house designed monolithic high-speed and high-gain photodiode. Each photodiode element consists of a plastic encapsulated fast photodiode with response time of 10 nsec.[17] The photodiode sensitivity curve is Cherenkov corrected by incorporating an upper band pass filter that rejects the light at the short wavelengths and transmits green light emitted by the excited scintillating centers. The fiber, photodiode

encapsulation, and filter are all plastic with a closely matched index of refraction to minimize interface reflections and consequently have higher sensitivity to the fibers' green light emission. The whole assembly is light tight and assembled using an in-house proprietary polymerization process to make a monolithic linear output radiation sensor with high efficiency and very low noise. The photodiode output is amplified by a high slew rate and high gain front end operational amplifier. The bandwidth is limited using a low pass RC filter to attenuate possible ringing oscillations and high frequency interferences that could be induced by the linac RF circuitry. The operational amplifier has a nominal gain of 10^3 and a Nyquist frequency of 40 MHz.[18,19]

C. Detector electronics

Clinical linacs deliver beams through high intensity pulse bursts carrying a large number of photons in a few microseconds.[20,21] Fluctuations in the pulse intensity come from the inherent fluctuations in the electron gun and linear accelerator pulsed network and operation.[20] The dose is controlled by integrating the pulses' energy in a large ion chamber and the pulse sequence is stopped when a predefined dose is reached.[20] Using this design, linac manufacturers average out temporal fluctuations from the feedback system controlling the dose delivered by each beam. To have an accurate detection of the linac pulsed output, a detector should have a large dynamic range and high bandwidth. The fiber array detector has the required large dynamic range to

acquire the high photon flux emitted by the scintillating fiber as a consequence of the high influx of gamma photons carried by each linac pulse. Furthermore, the photodiode and electronics have the required high slew rate and high bandwidth to accurately capture the true amplitude and shape of each ionizing radiation pulse.

The selection of a parallel detection and signal processing architecture is based on the need for real-time operation, which can only be achieved if each scintillating fiber has an independent signal-processing channel to store the instantaneous value of the fiber output generated by each linac pulse. At the detector analog subsection, high throughput is accomplished using a dedicated analog front-end amplifier and signal conditioning channel for each scintillating fiber sensor.

At the mixed signal section, real-time operation is accomplished using a synchronized sample-and-hold circuit in each signal channel that records the peak linac pulse value detected by each fiber sensor. A synchronous 120 channel parallel analog-to-digital converter reads the stored value in the sample-and-hold and the data is digitally converted and stored in the detector local memory. At the digital subsection, data is transferred to the computer between linac pulses before the next pulse arrival occurs. The analog-to-digital converter is a National Instruments data logger with 120, 12 byte channels

with the readout synchronized with the linac pulses. The triggering signal is constructed by summing the output from all fiber sensors. The data acquisition and signal-processing is accomplished by using an in-house LabVIEW program with real time visualization of the 120 parallel data acquisition channels. The estimated conversion time for this process is less than 10 μsec [8] and the data is recorded as time stamped vectors representing the output of each linac pulse event at each fiber sensor. A block diagram of the detector's main functional subsections is shown in figure 2. The software processes the output signal to determine the MLC leaf positions and compares this data with the expected detector output. Differences between the measured output and the expected output are used for real time treatment delivery error detection by comparing output differences every n linac pulses. The value of n is user defined, however n=100 is our practical value which is equivalent to verifying treatment accuracy every 6.5 cGy. This technique assures real time error detection and treatment cessation can be performed prior to any clinical relevant treatment deviation. This novelty enables corrective action by an automatic beam halting feedback system or by alerting a therapist.

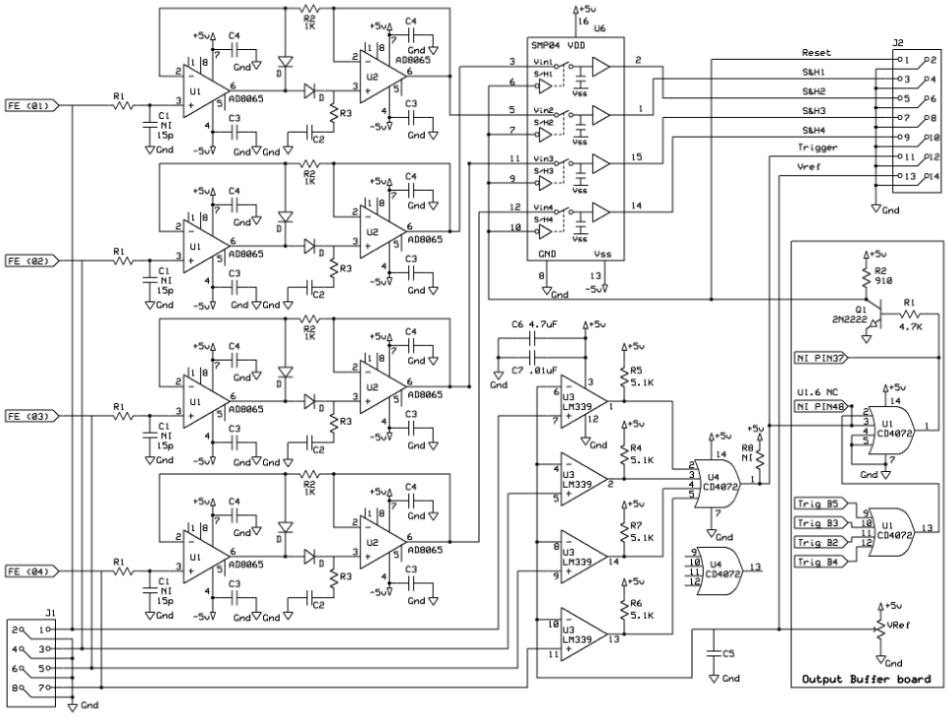

Figure 2. ***Detector Processing Electronics Schematic.***

D. Results

1) Test of the detector's overall operation and analog signal conditioning

We tested the detector operation by irradiating the fiber array with 6 MV and 18 MV photons with field sizes ranging from 5 cm to 35 cm. The output signal was evaluated at different key points in the detector processing electronics. In figure 2, we show a typical pulse at the output of the front-end amplifier and the sample-and-hold circuit. The variation of the pulse height shown in the sample-and-hold are due to variations in the linac pulsed output. Front-end photodiodes were tested to determine sensitivity and variability. Dispersion

between front-end stage outputs resulting from variations in the fiber to photodiode coupling where minimized by fine tuning front-end amplifier gain. Special care was taken to set the fiber gain to a level that prevents detector saturation during high dose rate bursts delivered by the linac. At the same time, the gain was selected to assure the minimum required sensitivity for discriminating field sizes with a resolution of 2mm or better. Residual variations were in the acceptable range of sensitivity dispersion and were compensated for by computing a calibration factor of each fiber sensor to achieve a homogeneous output for the linac 10x10cm^2 calibration field size.

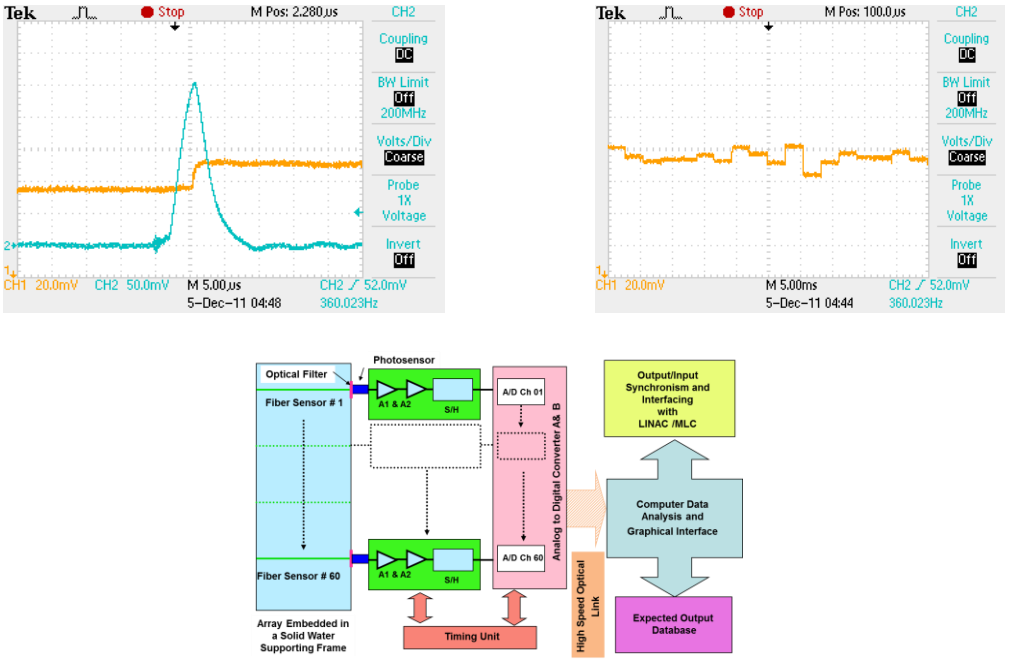

Figure 3. ***Detector Block Diagram and Pulse Processing Verification.*** Top left, output pulse from photodiode (blue) and sample-and-hold pulse (orange). Top right, sample-and-hold pulse train showing values of photodiode pulsed output over time. Bottom, detector signal processing and detector design is shown in the bock diagram and insets (only one side of the detector is shown for clarity).

As seen in the figure above, the pulsed output from the fiber array at both sides of the detector is conditioned and captured by the sample-and-hold in parallel and synchronous with the linac pulsed output. The pulse height sequence is digitally converted by a 120-channel parallel acquisition system (National Instruments) and then transferred outside the linac vault using a high-speed optical link. The host computer has an in-house developed graphic interface for real-time visualization of the detector data in different formats and comparison with expected data for error detection during treatment. Detector error signals can be sent to the linac controlling electronics for halting the treatment delivery if error signals cross the maximum error threshold set according to treatment technique and treatment site.

2) Fiber array calibration

Fiber array calibration is implemented to eliminate variations in the output from each fiber sensor channel and to dosimetrically calibrate each sensor with respect to the linac standard calibration field. Calibration as a function of the field size from 5 cm to 35 cm is quasi-linear and we found that a single calibration factor coefficient is required to calibrate each fiber. A look-up table can be generated for the array, assigning each fiber its specific calibration factor.

The calibration was performed by delivering 100 MU (100cGy) to the detector for field sizes ranging from 5cm to 35cm in 5cm steps across the fiber array using the averaged output signal of 100 linac pulses to provide a calibration independent of the intrinsic fluctuations of the linac output. The quasi-linear nature of the calibration factors is shown in figure 3 along with the calibrated detector output. Different calibration look-up tables are required for each energy which can be selected in the software.

For a consistency check, the fiber calibration is performed at the beginning of the day before taking measurements. Comparing the data to previous days, we can see if a fiber has been damaged or misplaced. This check also confirms that the detector electronics are functioning correctly.

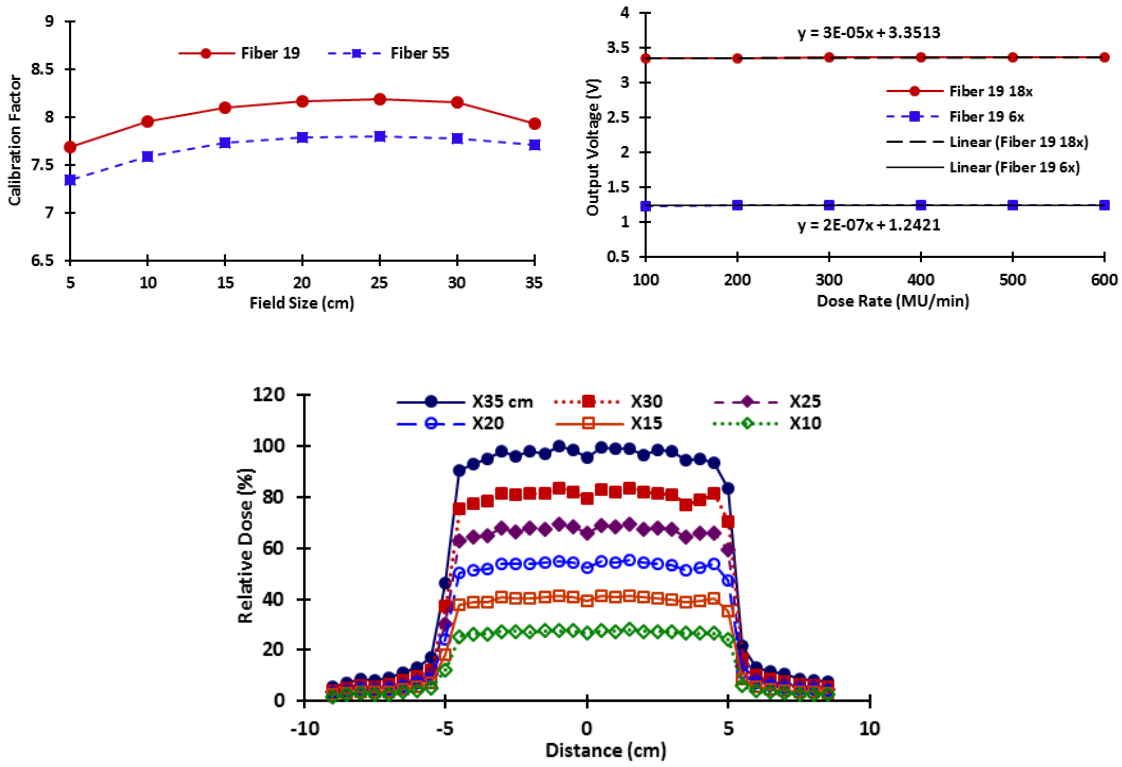

Figure 4. ***Detector Calibration.*** At the top left, calibration factors for two fibers as a function of the field size from 5cm to 35cm for a 6MV beam. Fiber response as a function of the field size is quasi-linear allowing single factor calibration for each fiber for a specific beam energy. At the right, a verification of the detector dose rate independency for a 6 MV and 18 MV beam is shown to be within a factor of 10-5 for all available dose rates. At the bottom, detector beam profiles for 10 cm beams (y-direction) from 10 cm to 35 cm (x direction). In this measurement, all profiles were captured using the result of 100 averaged pulses.

3) Dose rate independence in clinical energy range

The detector dose rate independence was tested as a function of clinically available dose rates of 100, 200, 300, 400, 500 and 600 MU/min and beam energies of 6MV and 18 MV. Both beams show no change in detector response as a function of dose rate within a factor of 10^{-5}(see figure 4, top right panel). An analysis of the detector time response shows that the front-end electronics time response was 0.2 µsec. This high-speed response is adequate to capture,

in detail, each 15 μsec linac pulse. Measurements of the pulse repetition show that pulses were delivered with a 16.66 msec pulse repetition time when the linac was operated at 100 MU/min, 8.33 msec at 200 MU/min, 4.16 msec at 400 MU/min, and 2.78 msec at 600 MU/min. We concluded that there is no detector saturation, pulse pile up, or missing pulses for all the clinically available dose rates and energies.

4) Crosstalk and detector alignment

Minimal fiber crosstalk is important to the detectors overall sensitivity and resolution. If surrounding fibers are receiving a signal, then false dosimetric and spatial information will influence the results.

The crosstalk was analyzed using a single fiber irradiation to measure fluence spill out into the two adjacent fibers and a complementary test of two fiber irradiation to observe fluence spill into a fiber between irradiated fibers. Measurements are reported in figure 5. It was found that crosstalk between adjacent fibers is limited to 2.2% for 6 MV and 18 MV beams in both tests, detector output and film measurements. Consequently, spill-out or the spill-in of the beam is generated by scattering in the MLC leaves and not by the detector inhomogeneities.

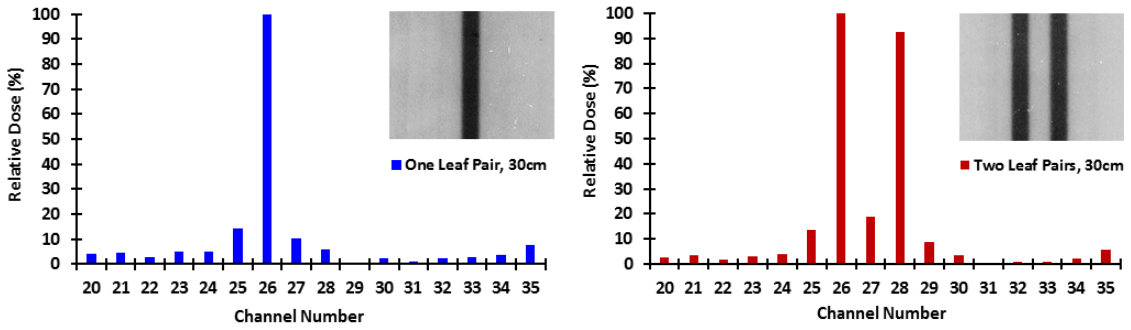

Figure 5. ***Crosstalk Between Adjacent Fibers in MLC Modulated Fields.*** The figures are for the single leaf and two leaf tests at 6 MV where either one leaf pair was opened to 30cm along the fibers or two leaf pairs were opened to 30cm.

5) Longitudinal resolution (x-axis)

The linear response of the detector output with respect to the linac x-jaw openings was found to have a linear correlation factor of 0.999 between the field width and pulse amplitude and fields defined by the MLC's show a correlation factor of 0.998. The data is shown in figure 6. A higher resolution analysis of the linear response, inset figure 6, shows the capability of the detector to sense beam width changes with 1.5 mm resolution in each MLC beamlet. Conservatively, we expect that during detector operation the detector will have an overall resolution and accuracy of 2 mm, which is within the 3 mm value recommended by the American Association of Physicists in Medicine (AAPM).[22]

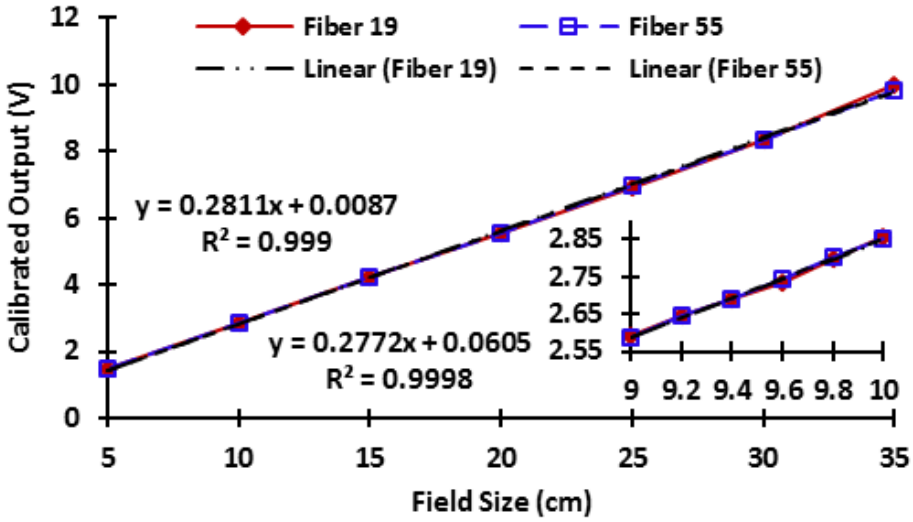

Figure 6. ***Linearity of Fibers with Respect to Field Size.*** Detector linear response with respect to field size with 5 cm steps in jaw position. Inset, high resolution analysis of detector linear response with respect to field size in 2mm steps from a 9 cm to 10 cm field. All detector fibers show equivalent linearity and field size resolution detectability.

6) Lateral or transverse resolution (y-axis)

With the MLC's and Jaw position set at a constant x position (along the fibers, see figure 1) resolution along the y-axis was tested to explore the use of fiber signal interpolation to achieve higher resolution than the 5 mm spacing of the 40 central fibers and 10mm spacing of the 20 lateral fibers. Figure 7 shows acquired beam profiles from 10 cm to 12 cm in 2.5 mm increments. Data shows a small amount of crosstalk from scattering between adjacent fibers, however, a consistent output allows systematic data interpolation to assure a lateral resolution of 2.5 mm in the 5mm spaced fibers region and 5 mm in the 10mm fiber spaced region, which is a resolution increase from the nominal lateral value by a factor of 2. Furthermore, this test shows the detector fibers' alignment with the beam isocenter or linac axis, and the MLC bank.

Noteworthy, setup was performed using the linac accessory tray slide and click system with no additional adjustments shows resolution and alignment reproducibility.

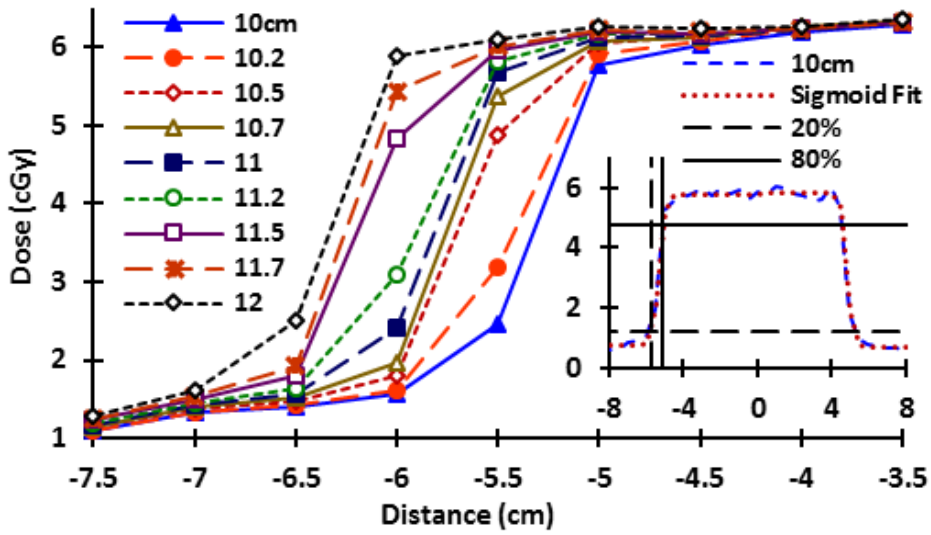

Figure 7. ***Lateral Resolution.*** Detector lateral resolution for a 6MV beam. All field sizes are kept constant at 10cm in the longitudinal (y) direction while the field size is varied from 10cm to 12cm in the lateral (x) direction. The data demonstrates the capability of the detector to resolve fields with a lateral field size change of 2mm; half of the fiber spacing or the nominal detector lateral resolution. The inset shows a calculation of the penumbra from 80% to 20% of a 10x10cm2 beam. Also included in the calculation is a stepwise sigmoidal curve fit to the detector output for calculation purposes.

A double sided sigmoidal fit was computed to determine beam size at half maximum and penumbra in the y-direction.

The double sided sigmoidal fit equations are:

$$\boldsymbol{S = \frac{A}{1+e^{-\propto(y+x_0)}} + C, if\ x \leq 0} \qquad \textit{eq. 1}$$

$$\boldsymbol{S = A - \frac{A}{1+e^{-\propto(y-x_0)}} + C, if\ x > 0} \qquad \textit{eq. 2}$$

Where A is the beam amplitude, α is the beam edge slope, and χ0 is the beam half width and C is the background, y is the distance from the beam center, and S is the output of the sigmoid function. Using this equation, the average penumbra in the transverse direction is estimated to be 6.26 mm +/- 0.88 mm for a 6 MV field 10x10cm^2 field and a beam width resolution of 2.5 mm.

7) Dosimetric calibration

The dose calibration curve showing the cumulative calibrated output with respect to a reference 10x10cm^2 field at 10cm depth (machine reference calibration) covering from 50 to 1000cGy is shown in figure 8. Data points for each beam were accumulated over time to record the total integrated detector output. Figure 8, shows the dosimetric calibration curve at set up. Linear fitting reveals a correlation of the cumulative detector output signal with central axis dose delivery with a linear correlation factor, R^2, of 0.9954.

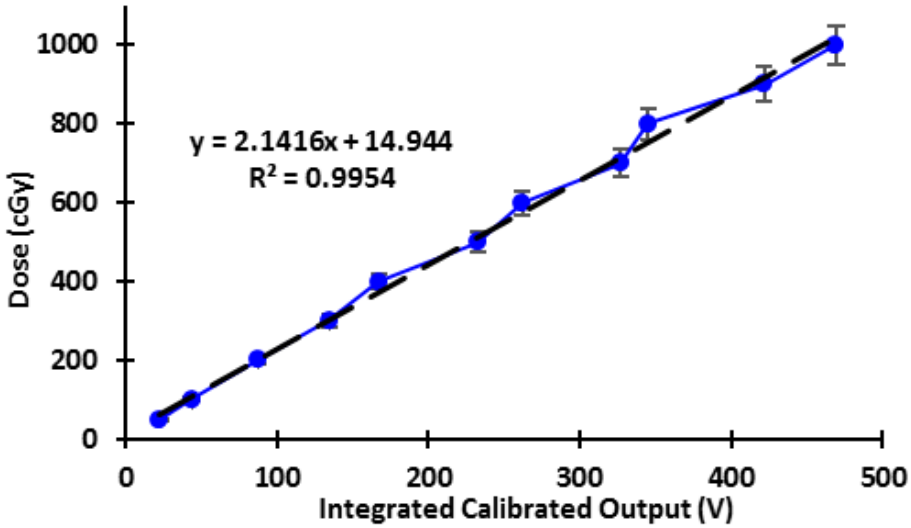

Figure 8. ***Dosimetric Calibration Curve.*** Cumulative output signal from the detector using calibration of the machine reference field at 6MV from 50cGy to 1000cGy at central axis. Calibration parameterization is subsequently used to compute doses. The data is presented with error bars of 5% to show that the data follows the linear model within 5%.

8) Verification of output calibration

The table below shows the results of three trials where the linac output was determined using the detector linear dose calibration shown in figure 8. The measured dose is compared to the machine calibration in a blind test reported in Table 1. The percentage of errors reported in the table are similar to the results of other blind tests, consequently a maximum overall error of 4.23% is used as an interval of confidence for future dosimetric evaluations.

Table 1. ***Verification of Detector's Reference Linear Dose Calibration.***

Dose Delivered (cGy)	880	550	130
Integrated Detector Output (V)	251.43	157.14	37.14
Predicted Measured Dose (cGy)	862.64	527.18	126.46
Percent Difference Dose (%)	1.99	4.23	2.72

9) Sensitivity

Detector spatial sensitivity is defined as the signal output change in mV per mm of field size change. This definition provides a method to quantify the instrument's capability to identify errors in the beam size and MLC leaf positions.

The spatial sensitivity ($Sensitivity_{Spatial}$) equation is:

$$\boldsymbol{Sensitivity}_{\boldsymbol{Spatial}}\left(\frac{\boldsymbol{mV}}{\boldsymbol{mm}}\right) = \boldsymbol{CF}\left(\frac{\Delta \boldsymbol{V_{out}}\,(\boldsymbol{mV})}{\Delta \boldsymbol{S}\,(\boldsymbol{mm})}\right) \qquad eq.\ 3$$

Where CF is the detector calibration factor, ΔV_{out} is the detector change in output voltage when a field size change, ΔS, occurs.

Dosimetric sensitivity is defined as the detector signal change in mV per cGy. This sensitivity provides a method to quantify the capability of the detector to capture errors produced by incorrect beam energy, output, and output rate.

The dosimetric sensitivity ($Sensitivity_{Dosimetric}$) is computed using the following equation:

$$\boldsymbol{Sensitivity_{Dosimetric}}\left(\frac{\boldsymbol{mV}}{\boldsymbol{cGy}}\right) = \boldsymbol{CF}\left(\frac{\boldsymbol{\Delta V_{out}\,(mV)}}{\boldsymbol{\Delta D\,(cGy)}}\right) \qquad eq.\ 4$$

Where CF is the detector calibration factor and ΔV_{out} is the change in detector output voltage when a dose change, ΔD, occurs in the linac output. Both sensitivities are weighted across the fibers' sensors using the detector calibration factors to achieve uniformity across the detector array.

a) Spatial sensitivity for step-and-shoot treatment techniques

The sensitivity of the detector with respect to beam size was measured for both jaw limited beams and MLC limited beams for 6 MV and 18 MV photon beams. For equivalent rectangular fields, jaw limited and MLC limited fields presented similar results. Spatial sensitivity was measured for 5, 10, 15, 20, 25, 30, and 35cm beam widths. In figure 9, we report the dispersion of the measured pulse signals as a function of the beam size for 8cm to 12cm fields and the average spatial sensitivity. The dispersion figure shows that a minimum of 2mm can be differentiated without false positives. The average sensitivity for 10x10cm^2 field shows that an analog-to-digital system with a resolution of 2mV will provide the required capability to match the statistical

limit of the 3mm with no false positives. These measurements were performed using total doses of 3Gy.

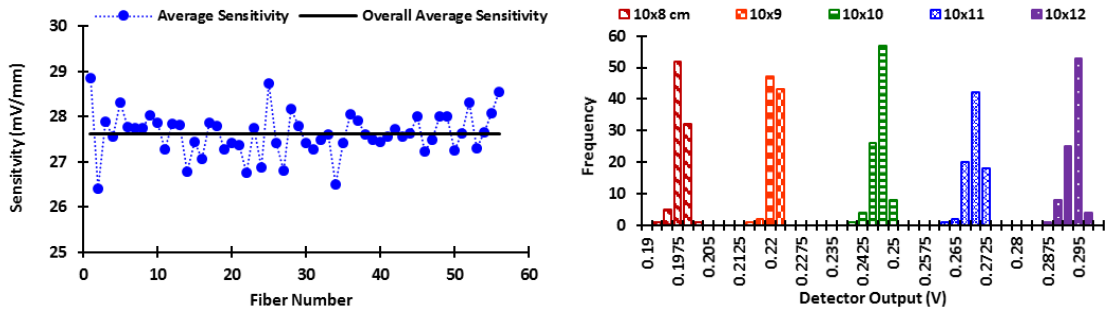

Figure 9. ***Spatial Sensitivity of Detector System.*** Left, residual dispersion of the average spatial sensitivity per fiber for 6MV and 10cm MLC defined fields. Right, histogram of the dispersion of the detector output in 1cm steps showing pulse statistics revealing no uncertainty in field determination with 3mm resolution.

b) Dosimetric sensitivity

The average dosimetric sensitivity of the detector was measured from 50cGy to 1000cGy using the dosimetric calibration curve in figure 8. The average dosimetric sensitivity was determined to be 454.61 mV/cGy. According to the A/D resolution of 25 mV (10V / 12 bytes) a dosimetric sensitivity of 1cGy to perform early detection of a treatment deviating from the planned dose to halt mistreatments is assured. Considering a typical 2-byte error the detector can capture 1cGy dosimetric changes from the expected treatment without false positives.

10) Time dependent output

The high speed parallel architecture of the detector allows the acquisition of every linac pulse and consequently the beam output as a function of time, therefore, the delivered dose can be traced as a function of time from the ramp up to the time when the total dose is delivered. In figure 10, we show the linac output as a function of time for a beam delivered with 400MU/min and a programed total dose of 600MU (6Gy). The figure shows the beam on ramp up followed by a slowly increasing output through time with fluctuations in the linac pulse output. This type of curve is consistent throughout the range of tested doses, from 50cGy to 1000 cGy.

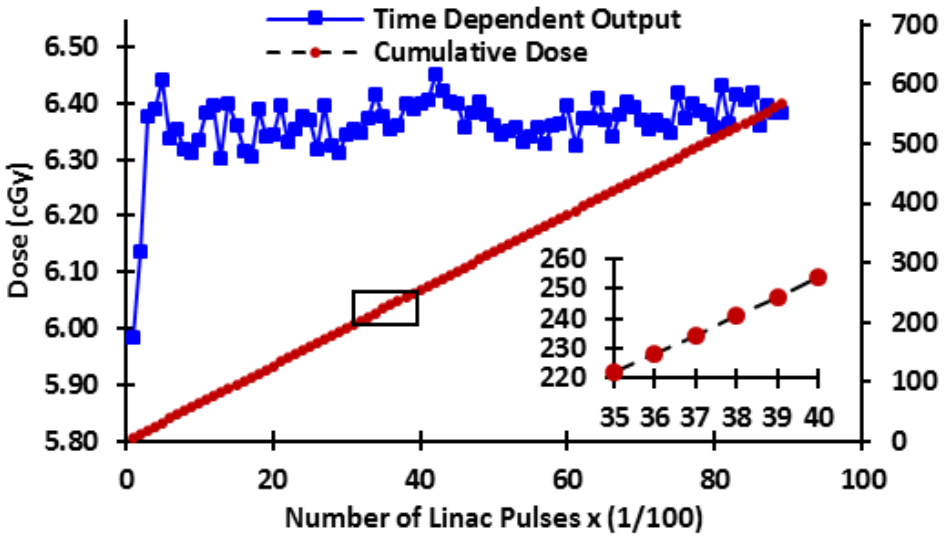

Figure 10. ***Linac Output as a Function of Time.*** Measured Linac output for a total dose of 600 MU, 400MU/min, 6 MV, and 10x10cm2 field. The dose vs. pulse traces are the averaged linac output every 100 pulses (blue) and the cumulative dose over time (red). The inset shows a close up of the cumulative dose to illustrate the smoothness of the cumulative dose despite the fluctuation in the output pulses.

11) Error detection

Validation of the detector's capability of sensing errors occurring during treatments from linac beam delivery malfunctions can be characterized, as follows:

A) **Spatial error:** beam shaping and modulation error due to jaw and the MLC positional errors.

B) **Dosimetric error:** unexpected change in the linac output such as incorrect energy, dose rate, or total dose.

12) Spatial error detection

A misplaced single leaf malfunction will produce the smallest output change, so we use this fault to determine the detector's spatial error sensing threshold. A single leaf was moved in and out of the field by 5cm, 1cm, and 2mm to simulate a single leaf MLC positional error respect to a 10x10 cm^2 reference field. In all cases, positional errors were detected, as reported in figure 11. A shift of 2 mm was determined to be the minimum detectable leaf misplacement without false positives. These measurements agree with the minimum error detectability established using the linac statistical dispersion reported in section 9.

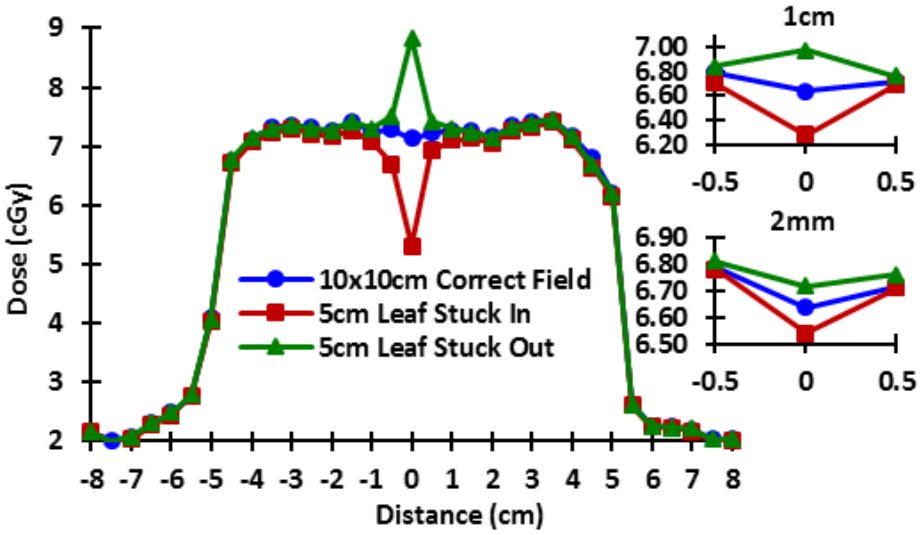

Figure 11. ***Detection of MLC Single Leaf Positional Errors.*** Figure shows a comparison between a 10x10cm2 reference field and the same field with a 0.5cm width MLC moved out of position by +/- 5cm, 1cm, and 2mm. The beam profile was measured using a central axis dose of 7 cGy to show the fast response of the detector.

13) Dosimetric error detection

To determine the sensitivity of the detector to resolve dosimetric errors originated by energy or output shifts a 10x10cm^2 MLC defined reference field was measured and the combined fluence and energy shift with respect to the calibrated beam was simulated by attenuating the beam. The attenuator created a 13 % output shift at the central axis reference value. Results are shown in figure 11, where the transverse profile of a 6MV beam is compared with the perturbed beam. The figure shows constant error sensitivity detection across the field width.

14) Beam collimation error detection as a function of time

Beam size error detectability was tested as a function of time for all time points of a beam in real-time of a MLC collimated field for a 10x10 cm^2 reference field and a putative error of 2 mm and 10 mm were recorded and displayed in figure 12.

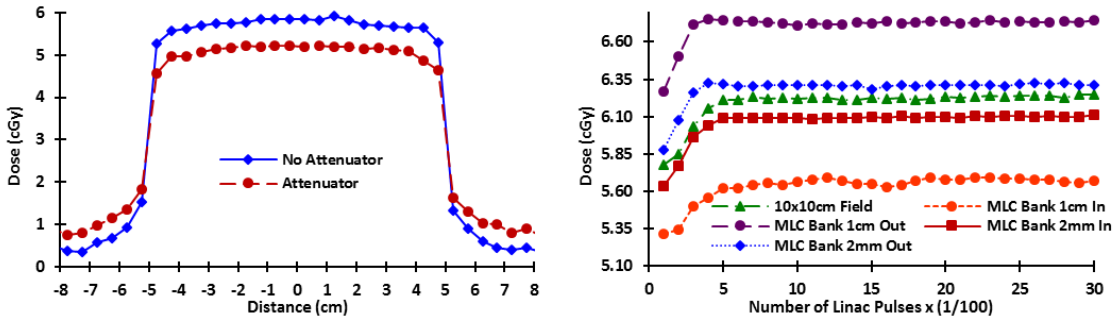

Figure 12. ***Dosimetric and Beam Collimation as a Function of Time Error Detection.*** Left, the figure shows the beam profile for a reference 10x10cm^2, 6MV beam collimated by the MLC's compared with the same field attenuated by 13% of the reference output to simulate a treatment error. Right, detection of positional error as a function of time for a standard 10x10cm^2 field compared to one bank of MLC's having a positional error of 1 cm and 2 mm.

Recorded time sequence data shows non-overlapping output for these fields as a function of time from the ramp up period and throughout the entire course of beam delivery. Consequently, the treatment field collimation accuracy can be recognized within 2 mm at any time of the beam on phase.

15) Treatment error detection

To provide a clinically relevant evaluation of the error detection capabilities, we performed blind tests for MLC error detection using a step-and-shoot IMRT prostate treatment. We simulated beam modulation treatment errors by misplacing a few leaves to positions causing 3% deviation of the intended dose distribution and by increasing the wedge angle by 5 degrees. Linac output measurements reported in figure 13 shows 100% error detectability across the field for both type of simulated errors Misplaced leaves were correctly identified according to their location and misplacement length.

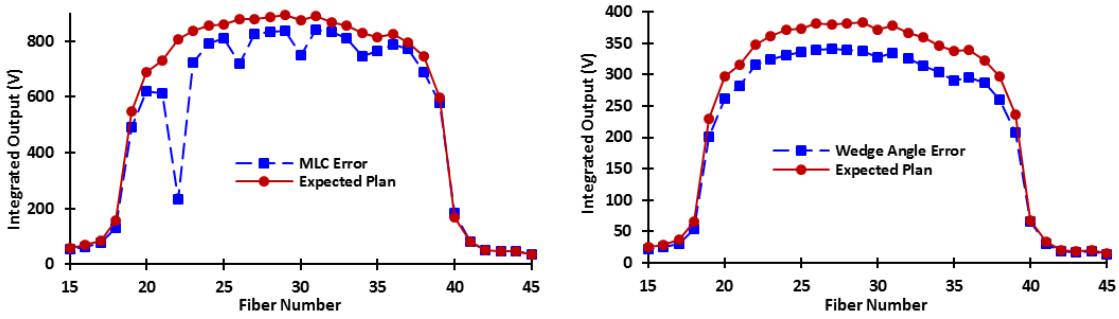

Figure 13. ***Error Detection in Step-and-Shoot Treatments.*** Left, detection of leaves 21, 25, 29, and 33 misplaced by 0.5, 1, 1.5, and 2 cm respectively. Leaf 37 was closed completely. The field used is an AP field of a conformal beam to a prostate PTV. MLC error test field is compared to the correct field. Right, comparison between wedge treatment fields for a prostate plan with the same field with a wedge angle error of 5 degrees.

To test the capability of the detector to monitor treatment plans during delivery and to capture dosimetric errors in real time, a generic rectum treatment plan with and without treatment faults was delivered to the detector. Output errors were induced by reducing the number of MU's by 10

units (3% of beam dose) in one beam and spatial errors were introduced in another field by randomly selecting and misplacing MLC leaves by 5mm or less. To a plan reviewer, the dose distributions are almost indistinguishable, however, the detector output as a function of time reveals high sensitivity to capture errors in real-time, as reported in figure 14.

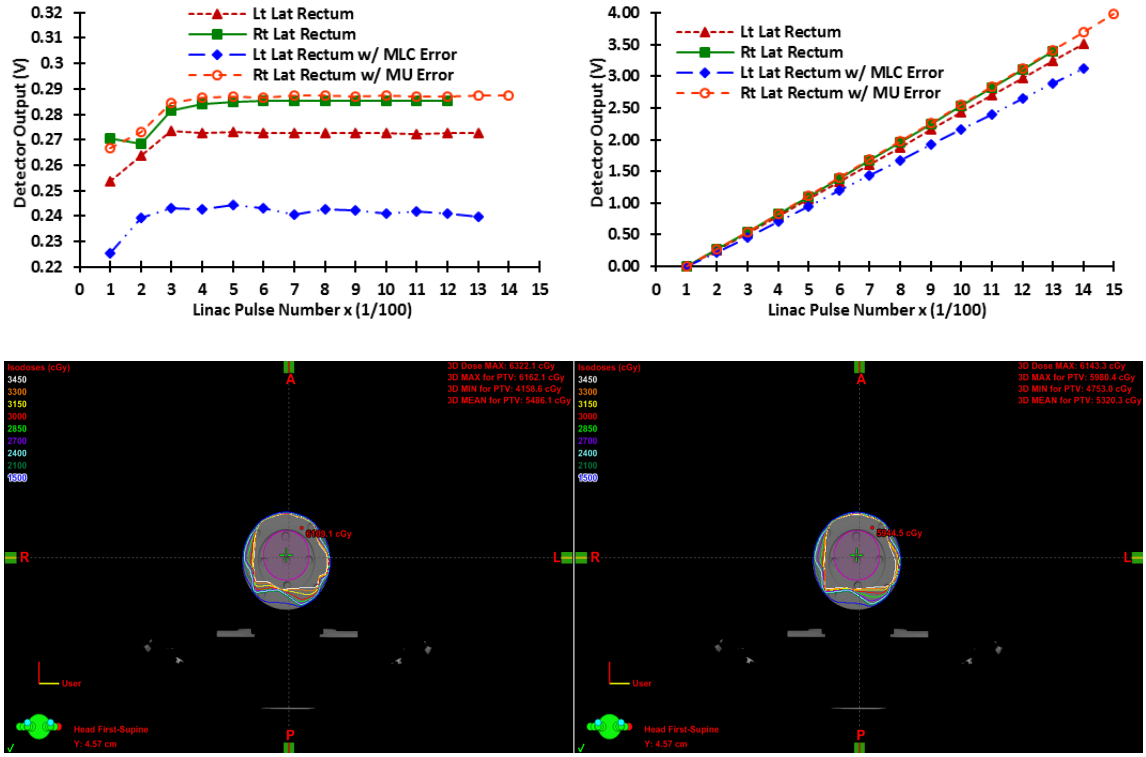

Figure 14. ***Step-and-Shoot Real Time Error Detection.*** Top left, figure shows detector output as a function of time for the planned left lateral and right lateral fields and same fields with output (Rt Lat Rectum field) and spatial delivery errors (Lt Lat Rectum field) for a rectum plan. Each point corresponds to every 100 linac pulses. Left field traces show a change in the detector intensity at all times reflecting different MLC leaves positioning and a right field comparison shows the same track but with longer delivery time or point reflecting a change in total output. Top right, shows the integrated output over time. It is possible to see when the treatment deviates from the planned treatment. Bottom left, screenshot of the dose distribution from the treatment plan with errors; and bottom right, the correct plan, as presented to a plan reviewer. The isodose and the PTV both show indistinguishable features to a plan reviewer.

The data and TPS dose images demonstrate the detector's high sensitivity to capture dosimetric and spatial errors in real time even when there is only a subtle change in the delivered fields. As a function of treatment time, the detector output data shows that slight deviations in the MLC positioning can be captured in real time during the delivery. In addition, time sequence data shows that output error can be detected by tracking the treatment length or the cumulative output and it is possible to monitor the individual MLC time trace by looking at each fiber output to uniquely determine which MLC leaf pair is causing beam modulation errors. For both errors, an alarm system can be triggered to alert the therapist without false positives using the cumulated error in detector output which is proportional to the erroneous dose delivered to the patient.

E. Analysis and discussion

The detector realization is based on the use of a high sensitivity monolithic fiber sensor array with parallel electronic data processing, conditioning and acquisition. The detector is assembled using a substrate that is machined to have a minimum beam perturbation, absorption and scattering during treatment delivery. These characteristics allow the detector to operate in transmission mode for the duration of each treatment. The Cherenkov light originated by the slowdown of the high energy electrons is spectrally rejected using a combination of plastic photodiode encapsulation and polymer filters.

The detector is mounted on the linac accessory tray and centered with respect to the linac beam axis requiring no additional care than the traditional tray set up for blocks and wedges. All of these characteristics made our detector a highly versatile, compact and low-cost implementation.

Validation of the detector was performed with varying beam widths, intensities, and dose rates. Testing included increasing MLC widths along the fiber lengths to verify the linear response of the signal output with beam dimensions covering the practical range of the most commonly MLC modulated clinical beams, including carriage shifts. We tested our technology for dose rates covering the complete range available in a clinical linac (100 to 600 MU/min) to validate real-time device output accuracy and to assure a device that is versatile enough to provide real-time dosimetry for all linac treatment options. Beam energies used in our tests included 6 MV and 18 MV photon beams, however other energies will show similar linearity and detector dosimetry accuracy when it is calibrated according to energy and dose rate using look up tables.

The data reported in the previous section shows adequate resolution and precision to determine beam fluence and beam modulation departures from the computed treatment plan according to tolerances recommended by the AAPM for external beam radiotherapy.[22] An important result of this work is that our

fiber based sensors can detect each pulse delivered by the linac at all available clinical dose rates and clinical beam energies with high sensitivity to errors. Consequently, our detector technology is capable of sensing beam departures from the expected treatment when only a small fraction of a beam is delivered. This is important to prevent an inaccurate delivery of a clinical relevant dose to a patient. Through simultaneous testing of multiple closely aligned fibers, we have demonstrated that there is minimal cross talk between adjacent fibers and beamlets which means that complex beams with highly modulated profiles can be resolved. This result verifies that the fiber coating and optical couplings have the quality and integrity to effectively eliminate ambient light and light from neighboring fibers. Using all plastic materials, Cherenkov noise was suppressed to undetectable levels using spectral discrimination without significantly reducing the light output from the fibers.

The cumulated error signal provides a faithful method to stop treatment before mistreatment occurs, thus providing a higher level of patient protection and dosimetric treatment delivery accuracy. These operational characteristics were validated in this article by testing the sensors using photons, however the detector's capabilities can be extended to electrons showing that our real-time dosimeter array is a highly versatile dosimetry device for both treatment modalities.

A practical perception of how our real-time fiber detector can improve patient safety can be understood through the following example. Consider a patient being treated with a 10x10cm^2 beam delivering 2Gy to a PTV located at a depth of 10cm using a linac calibrated at 1MU=1cGy and there are approximately 1000 linac pulses per 1Gy. From the data reported above, we can conclude that we can easily detect a positional error of 1cm in a single MLC leaf with a width of 0.5cm. This leaf error will only contribute to 0.5% of the total beam which is only 1cGy of the 200cGy. In a 30 fraction treatment, the accumulative dose error will be 30cGy. The detector records the average of every 100 linac pulses to eliminate variations in the output due to the inherent noise of the linac pulsed forming network. Under these considerations, the detector can capture an MLC positional error with 5% of the beam being delivered. This would mean that only 10cGy would have been delivered and only an error of 0.05cGy would have occurred. Assuming this error occurs once every fraction for 30 fractions this would lead to only 1.5cGy being delivered in error.

A point of discussion is that at this discrimination level there are going to be many false positives. However, here is where the sensitivity of the detector can play its role and the data in sections 3.8 – 3.10 show that the possibility of false positives is close to null. Furthermore, to avoid false positives the cumulative error signal can be used to set thresholds according to experience and machines used in a particular clinical facility. These thresholds can be set by software to

confidence levels according to experience to weigh patient safety with false positive errors and according to treatment complexity or treatment technique.

In real time operation, the detector output is normalized and calibrated at the central axis with respect to a reference beam of 100 cGy using the dosimetric calibration curve shown in figure 8. Calibrated output time sequences are compared in real-time with the expected output previously computed using the treatment plan and detector sensitivity. If the detector output deviates from the expected sequence, at any portion of beam delivery, the departure from treatment delivery can be inferred, and the current and subsequent dose error can be determined. Thresholds are used to avoid false positives and are selected taking in consideration noise, and clinical relevance using as a guide the AAPM maximum 3% and 3mm dose and distance agreement rule. The dosimetric curve can be used in conjunction with the spatial calibration of the detector to identify spatial modulation treatment errors. The demonstrated sensitivity shows the detector's capability to recognize jaws and/or MLC's out of the planned position as small as 2 mm with a response time of 25 milliseconds.

F. Conclusions

The feasibility of constructing an imaging dosimeter capable of enhancing patient safety during treatment delivery and recording the true beam delivered

dose based on the scintillating sensor technology tested in this article depends upon the precision and accuracy of the fiber sensors to measure the MLC positioning error, delivered dose, and dose rate output linearity. The results of these tests showed that the designed imaging dosimeter will operate with the required linearity, sensitivity and precision to determine errors in the beam doses, sizes, and energies typically encountered in clinical treatment protocols.

III. THE SRS/SBRT SCINTILLATING FIBER DETECTOR

A. Detector construction

1) Overview

The detector consists of two scintillating fiber arrays that are embedded in an acrylic matrix. The fiber arrays are embedded in a substrate to produce a homogenous density detector with a thickness of 5mm. The small thickness of each array allows for the detector to be highly radio-transparent and to produce minimal scattering for megavoltage photon beams. The two arrays are arranged so that the scintillating fibers are orthogonal to one another to create an X, Y plane. The plane created by the arrays is perpendicular to the beam. Each array is coupled to a set of photodiode arrays to read the emission at both ends of the scintillating fibers to acquire complementary data. Each photodiode array consists of 128 photodiode sensors with a center-to-center spacing of 0.8mm. The pitch of the photodiodes in the arrays and the fibers are matched one-to-one. The fibers are coupled directly to the photodiode via simple direct contact. Photon loss is minimized by utilizing a photodiode that is slightly larger than the fibers so that all light leaving the end of the fiber interacts with the sensor. The photodiode arrays are designed to avoid noise from external sources, and consequently, they are spectrally tuned to maximize the response in the green portion of the spectrum and to reject the near infrared and deep

blue, leaving only the far edge of the Cherenkov emission that can be rejected using a variable threshold. In addition, the composition of the fibers is such that the scintillating light produced in the fiber is emitted in the green emission range. This enables the detector to filter out the Cherenkov light without losing data.

The arrays read in parallel, and each array has serial output with a total reading time that is dependent on the main clock of the driver circuit. The analog output of each pixel is digitized by reading the plateau of each pulse in a boxcar pulse sequence. Analog-to-digital conversion is performed using a data acquisition system from National Instruments. A LabVIEW program controls the data acquisition sequence, performs analysis of the data, performs an initial beam reconstruction, and records the output from each detector. The detector arrays are an integrating-type system, and the measurement is asynchronous with the linac pulse sequence. The integration time is controlled by the photodiode array driver circuit and can be adjusted to the time desired. For this application, the integration time is adjusted to that the integration period captures approximately 100 pulses of the linac output.

This detector is unique because it employs the use of a mechanical rotation system that allows the detector arrays to rotate 360 degrees to reconstruct radiation beam profiles. The data acquisition reading clock is in

synchronization with the rotational system so that measurements can be collected at precise angular locations to acquire projections of a radiation beam profile with certainty between directional and temporal coordinates. To reconstruct a beam profile, a minimum of 15 projections is required, which consist of 180 degrees of rotation in a time frame of 1 second. The rotation is controlled by a stepper motor that can provide an angular resolution of 0.01 deg per step +/- 5%.

The assembly has two arrays for two purposes, A) to perform a static measurement for beam tracking with more data points than a single array and B) to perform full reconstruction of a radiation beam profile utilizing multiple projections of a modulated field with a sub-millimetric resolution. Other commercial devices with the real-time tracking and one-dimensional data can detect errors with a precision of 3% and 3mm. However, there could be some unresolved correlation between the MLC positioning and the data. Therefore, by using two arrays, we have determined that the uncertainties will be null.

2) Detector electronics

The photodiode arrays are controlled by a driver circuit that requires an input of a 0V to 5V digital timing pulse sequences to control the integration time. The arrays also trigger the electronics to begin integrating and collecting the output from the scintillating fibers.

The first input pulse required is the M-CLK pulse or the pulse that controls the overall timing of the device. All the other required input pulses must be synchronized with this clock pulse for the device to function properly. The second input pulse required is the reset pulse. This pulse has two purposes as the digital pulse rises and falls. When the pulse rises to 5V the detector begins integrating, storing the data collected by the photodiodes. It is important to mention that there is a delay of 8 M-CLK pulses before the driver begins integrating, and the driver continues to integrate if the pulse remains high. When the pulse falls to 0V, the driver begins to stop integrating, but again, there is an 8 M-CLK pulse delay before the integration stops. After 17 M-CLK pulses, the driver outputs a boxcar waveform. This waveform is a series of 128 analog pulses that represent the response from the photodiodes to light over the time of integration. For every output pulse in the boxcar waveform, another digital pulse is generated called the trigger pulse. This pulse has no data value; however, it is a means to synchronize the data acquisition device to the driver output so that further data processing can take place. Finally, there is an end of scan pulse. This pulse is emitted, as the boxcar waveform ends, to signal that the data from the last integration time has been sent, and the next boxcar waveform will be a new data set from a new integration time. The cycle repeats. A summary of the input and output waveforms is depicted below.

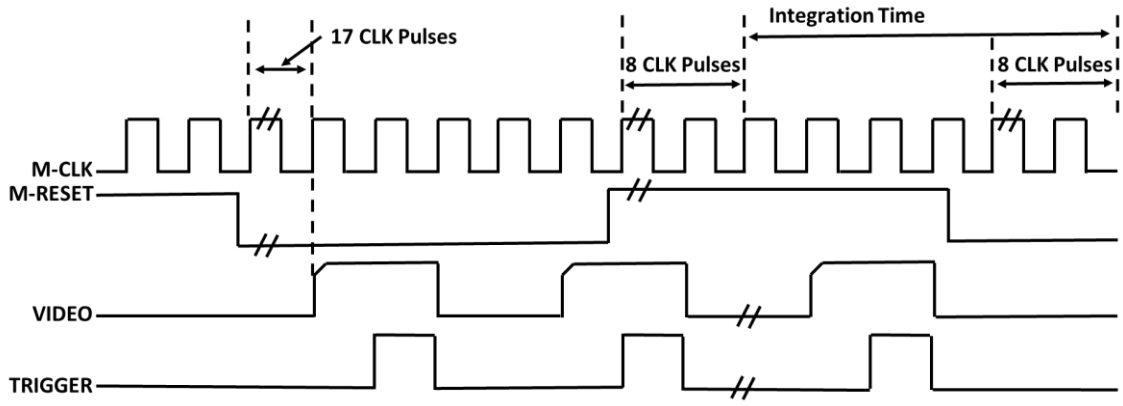

Figure 15. ***Photodiode Driver I/O Pulses.*** This is a summary of the input and output pulses for the driver circuit.

The driver timing circuit is composed of several analog devices. The master clock is driven by 1 MHz crystal oscillator. This device generates the pulse required to control the timing of the circuit as described above. The crystal oscillator then goes directly to a buffer. The oscillator also connects to several counters. These counters are used to divide the clock pulse down to the desired period used for the integration time. In this case, 8ms was determined to be the most useful value. This value is most useful because the integration time is long enough for the driver to collect the response of the photodiodes from small radiation fields but short enough that the driver does not saturate with radiation fields up to 10cm x10cm. This pulse is then sent to a 555 timer that is operating in monostable mode. The output from the timer is used to create the m-reset pulse by determining how long the output pulse remains high so that the desired integration time is acquired.

The circuit simplicity allows a robust and easily reproducible electronic timing circuit. A robust circuit is important because there is a large amount of

electromagnetic interference in the linac vault when the linac is operating. In addition, the components are discrete devices which tend to be more resistant to radiation damage than larger integrated circuits if the electronics pass through the radiation field.

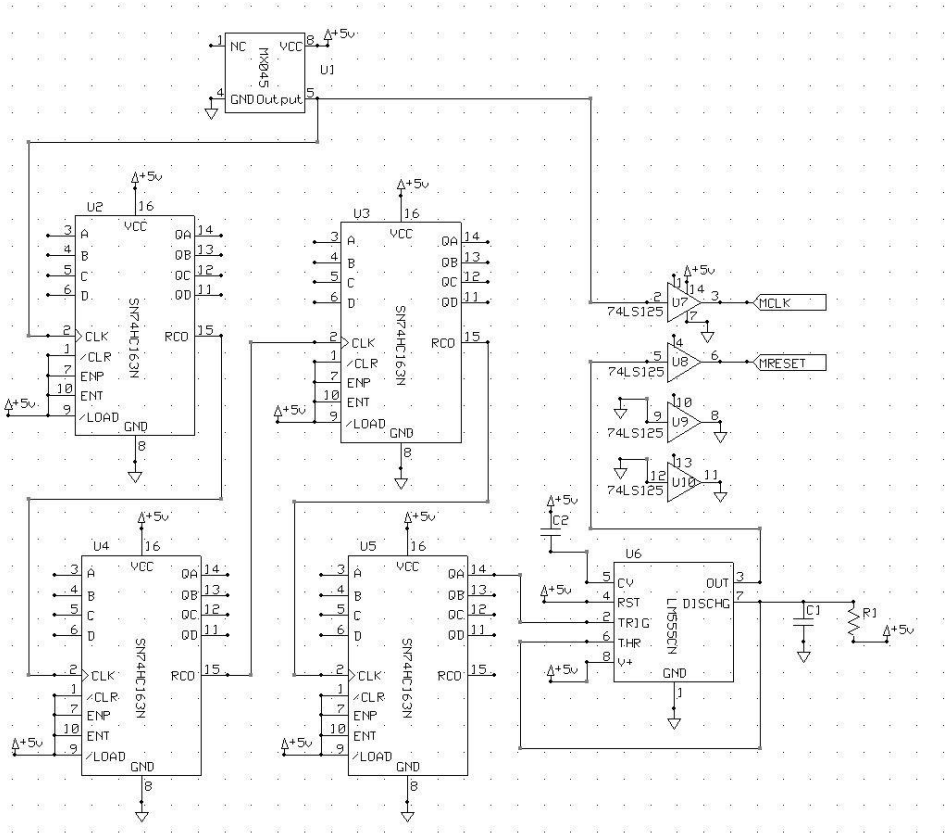

Figure 16. ***Schematic of Driver Circuit.*** The driver circuit is used to control the photodiode arrays.

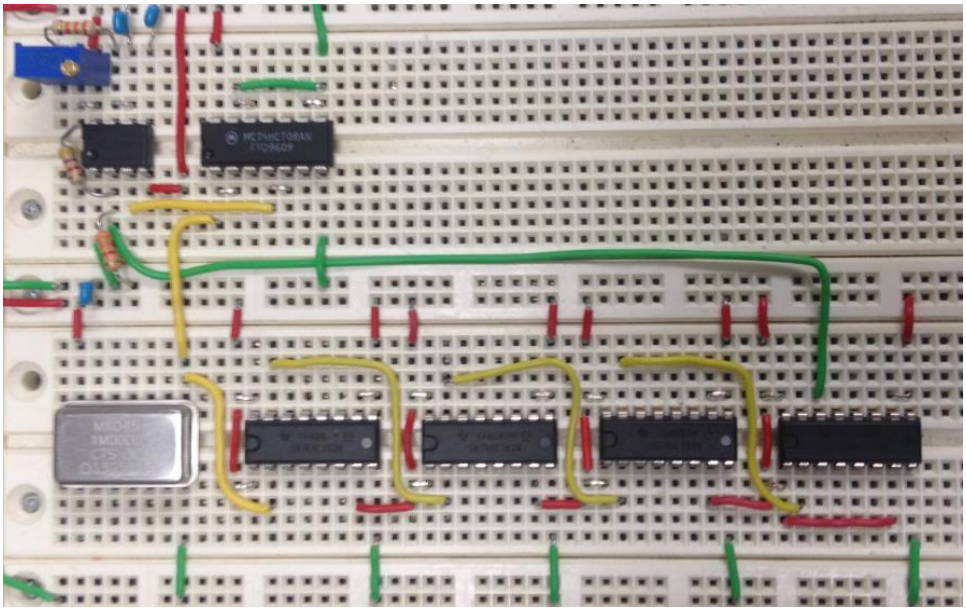

Figure 17. ***Prototype Driver Circuit.*** This photo depicts the prototype circuit developed to determine the optimal integration time.

A prototype of the driver timing circuit was first constructed using a breadboard (or protoboard). This circuit allowed for the integration time to be controlled by a potentiometer to vary the resistance in the 555 timer circuit; thus, allowing the ability to adjust the high time of the reset pulse.

3) Detector proof of concept prototype

The first prototype of the detector was constructed using a simple acrylic frame with nylon screws to limit the amount of radiation scattered by the support materials. The scintillating fibers were then mounted to the acrylic bed using double sided tape and a small amount of cyanoacrylate glue. The spacing of the fibers matched the photodiode spacing so that the fibers would have the best opto-coupling possible. The photodiode array and driver circuits were

attached to the frame by nylon screws so that both ends of each fiber had a photodiode coupled to it. This setup proved effective for proof of functionality, and the device was capable of detecting small radiation fields of 0.5cm x0.5cm delivered by the linac. The first prototype is seen in the figure below.

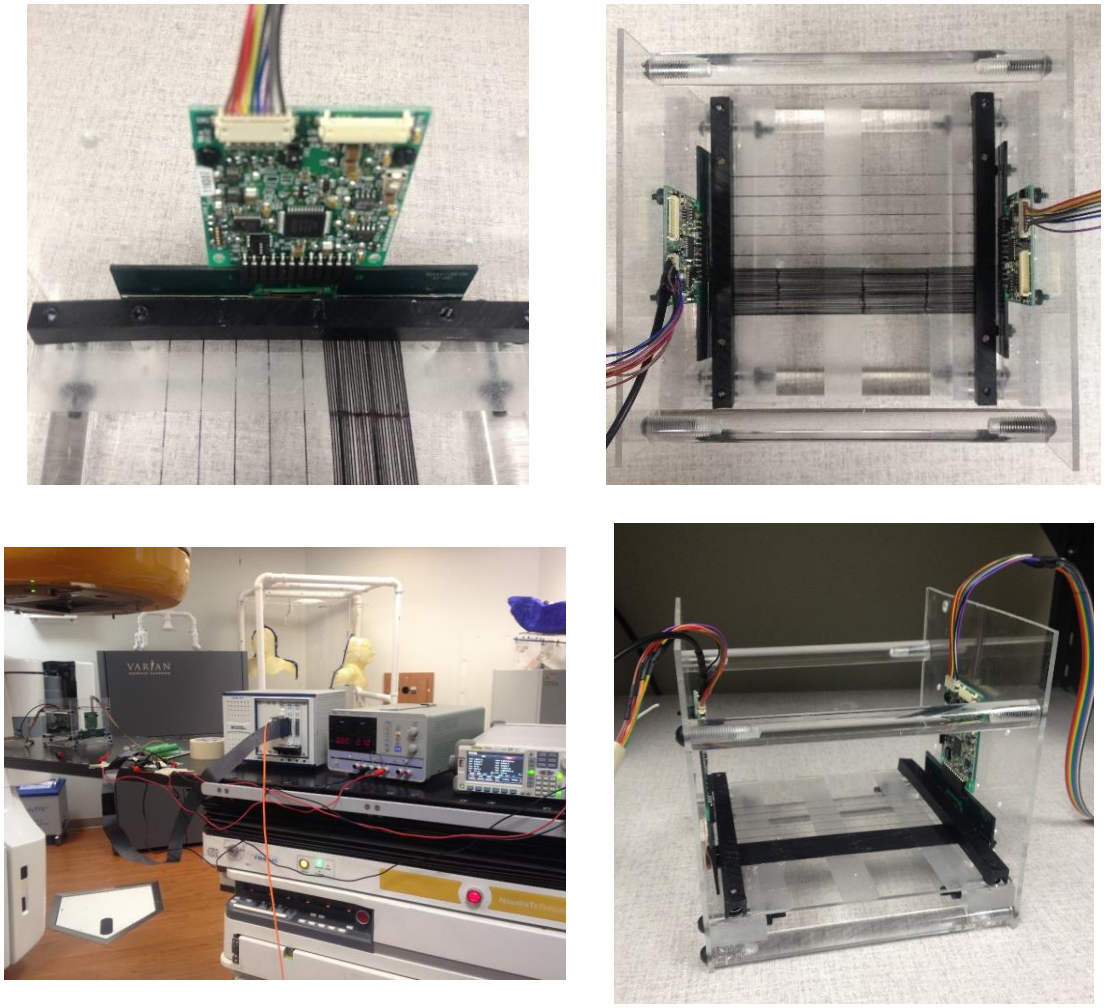

Figure 18. ***Prototype Detector System.*** Top Left, photo of driver board and photodiode array and test fiber array. Top Right, photo from above of test fiber array coupled to opposing detector arrays. Bottom Left, photo of detector system setup on Varian Novalis linac. Bottom Right, photo of detector from side.

4) Final implementation of detector

The second detector design was ultimately used for the final construction. The majority of detector's structural parts were planned and created using 3D CAD software and 3D printers. The core detector electronics remain the same with the exception of adding two more photodiode arrays and two more driver boards. The timing circuit also remains the same except for removing the potentiometer on the timing circuit, and replacing it with a fixed value resistor. Using a fixed value resistor ensures a more reproducible setup and removes the possibility of the resistance inadvertently being modified in the 555 circuit.

The timing circuit was reconstructed using a solder prototype board. Soldering directly to the electronics board to improves the reliability of the system, reduces noise in the signals, and decreases the size of the circuit. The figure below depicts the improved timing circuit design.

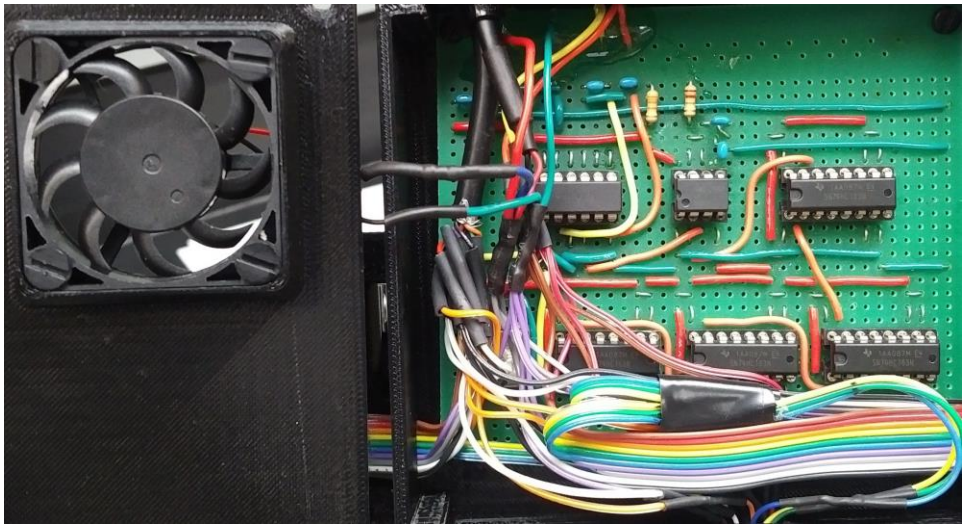

Figure 19. ***Final Driver Circuit.*** This is the improved circuit developed to use for the duration of the tests.

The final circuitry was then tested several times over many hours to ensure its reliability. Test results showed that the electronics needed to be energized and left to warmup for 15 minutes before data should be collected. This warmup time is needed due to the reset pulse high time changing as the resistor temperature increased in the 555 timer circuit. If the integration time is not consistent, then the data cannot be accurately analyzed after each test. Overall, the timing circuit performed as expected, and it was determined that it would be used for the final design.

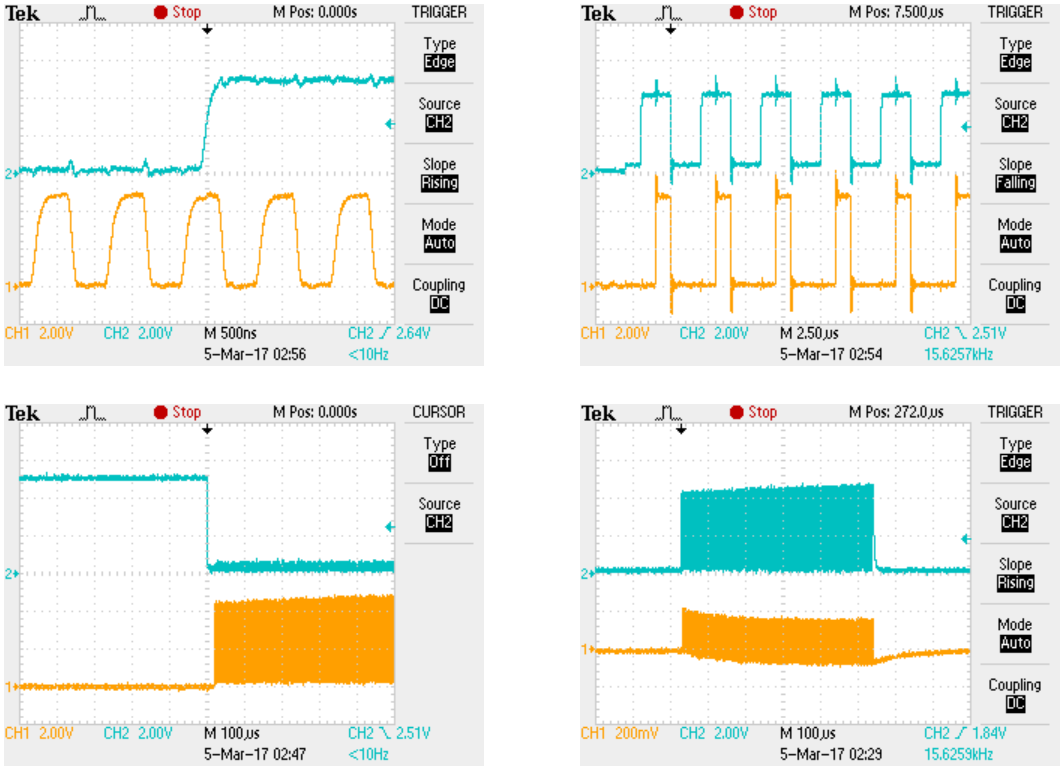

Figure 20. ***Typical Input/Output Pulses.*** Top left, display of the reset/integration pulse (blue) and clock pulse (orange). Top right, boxcar output of photodiode response data (blue) and trigger pulse for individual photodiode output (orange). Bottom left, the reset pulse falling low (blue) and the boxcar data output beginning after short delay (orange). Bottom right, saturated boxcar output (blue) and individual photodiode trigger pulses (orange).

5) Final structural fabrication

a) Fiber substrate

The first structural component developed for the final design was the substrate in which the fibers are embedded. To create a strong support for the fibers a 2mm thick acrylic sheet was chosen. The dosimetric properties of acrylic are similar to water and is also easy to machine. First, grooves were cut into the acrylic sheet using a small sword engraving bit and CNC milling machine.

These grooves are for the fibers to lay in so that they are evenly distributed and aligned with each photodiode. The gcode required and machining was completed in-house. The next task was laying the fibers along the grooves. All 128 fibers were fixed at both ends and in the center with a small drop of cyanoacrylate glue (CA). This glue was chosen because sets quickly and adheres to the scintillating fibers and the acrylic substrate. A mold was constructed out of clay around the perimeter of the fiber substrate, and a two-part epoxy was poured over the fibers so that they became embedded in the substrate. After the epoxy had fully cured, the fiber array was removed from the mold and placed on the CNC machine. The edges of the fiber array were then refined using a deburring mill bit to remove any excess epoxy and to remove any length of excess fiber.

The fiber ends were then polished using a specialized fiber optic polishing kit. First, the fibers were wet sanded using a coarse 3 μm abrasive material to remove any deep scratches in the fiber surface. Then, through several iterations of wet sanding and fine abrasives, the fibers were polished to achieve the desired result.

The new array is a major improvement over the previously tested prototype array. The fiber arrangement is more uniform and each fiber is fixed in position so that they cannot move. Calibration of the detector is easier because once the

fibers are coupled to the photodiodes they will not shift from position. In addition, the measured detector data is more accurate due to the fibers following a precise linear channel.

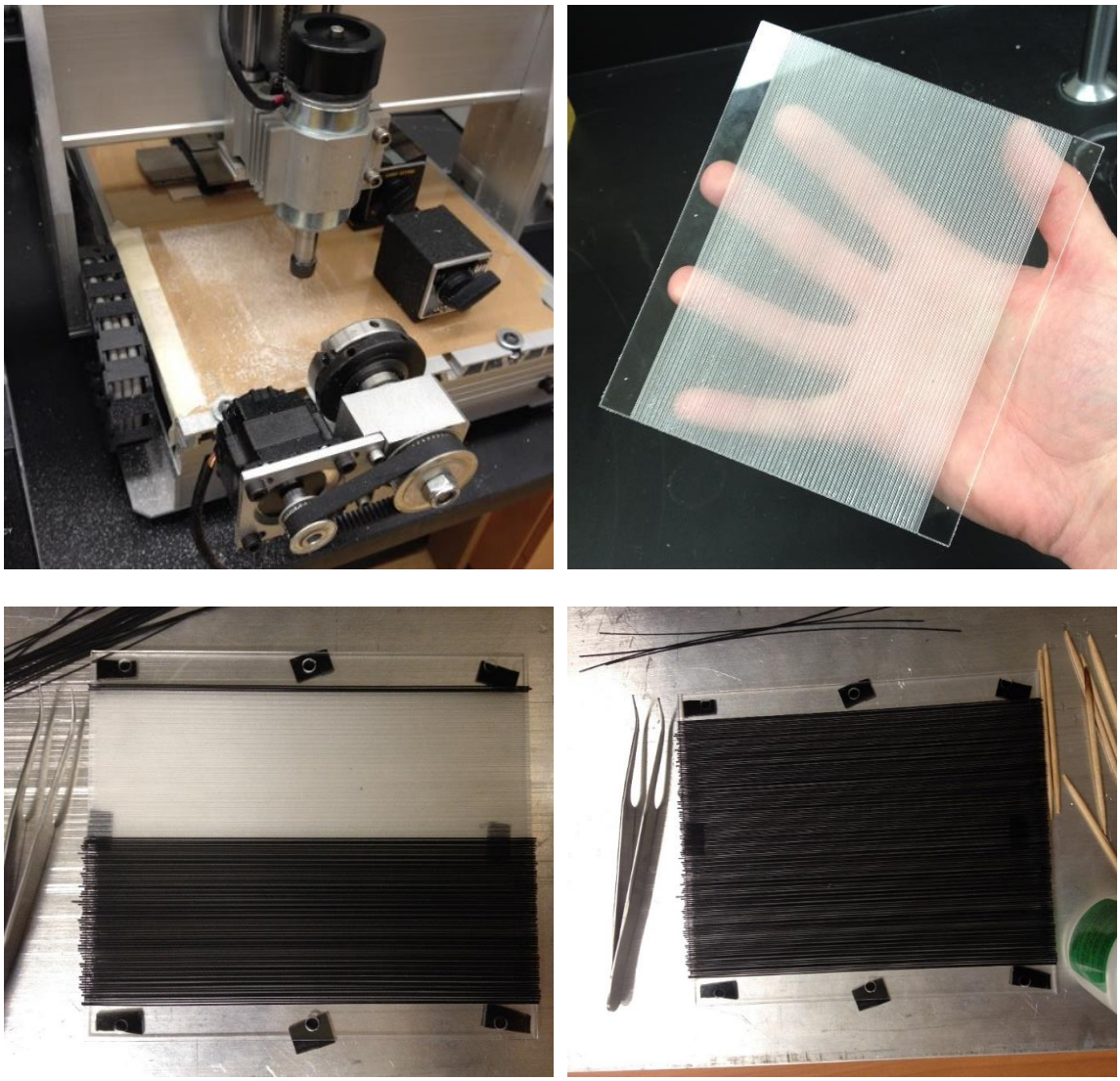

Figure 21. ***Scintillating Fiber Array Construction.*** Top Left, photo of CNC machining the fiber array substrate. Top Right, photo of finished fiber array substrate. Bottom Left, photo of laying fibers on to substrate. Bottom Right, photo of completed fiber placement.

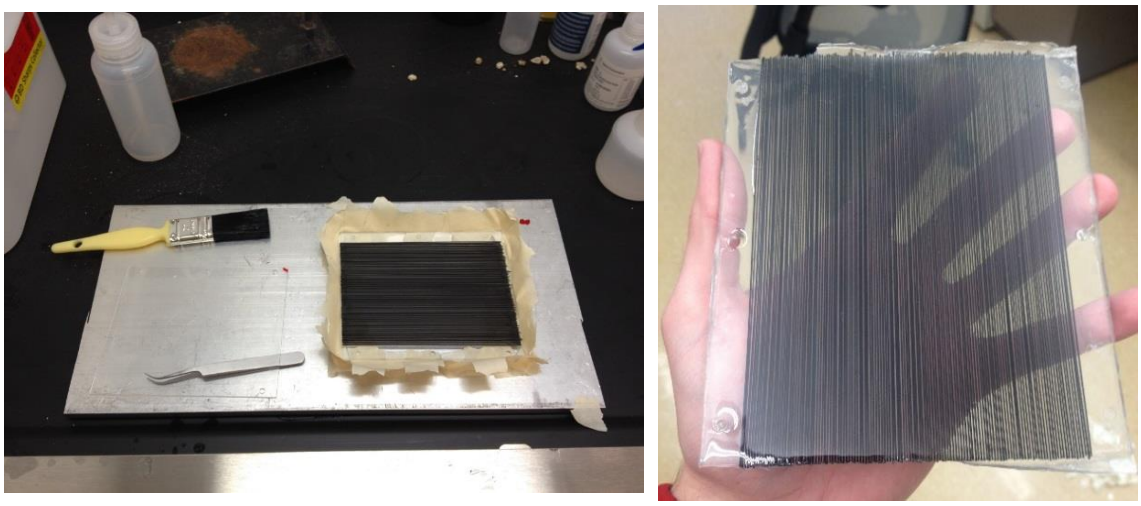

Figure 22. ***Embedding Scintillating Fiber Array in Polymer.*** Left, photo of fiber array of mold for pouring polymer coating. Right, photo of fiber array removed from mold.

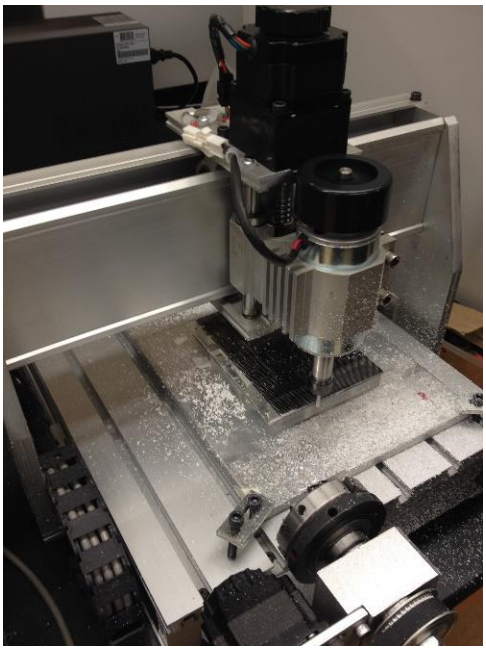

Figure 23. ***Completing Fiber Array.*** Photo of CNC machining array after polymer coating.

b) SBRT/ SRS detector structure

The remaining support structure of the detector was designed using a 3D CAD software. Each part was specially designed in-house and created using a 3D printer. The 3D printed parts were desirable due to the convenience of manufacturing the parts. Also, the honeycomb structure of a printed part allows for the detector to be very light weight but also very strong. The plastics used for the construction of the detector were PLA and ABS. These plastics will not significantly attenuate the radiation beam and will produce minimal scattered radiation.

The design of this detector is unique because it can rotate up to 360 degrees. This rotational freedom is so that the detector can scan a beam profile and reconstruct the shape for high-resolution machine quality assurance. To enable the detector to rotate freely a large bore ball bearing ring assembly was used. The bearing assembly is made from steel. However, it is very thin, and the beam should never pass through it, nearly eliminating any contamination from scattered radiation. Next, to control the rotation of the detector, a small NEMA-8 stepper motor was installed. The motor is connected to a small timing pulley and belt that connects to a large timing pulley on the detector. As the stepper motor turns, the detector rotates in a clockwise or counterclockwise direction to scan the beam profile.

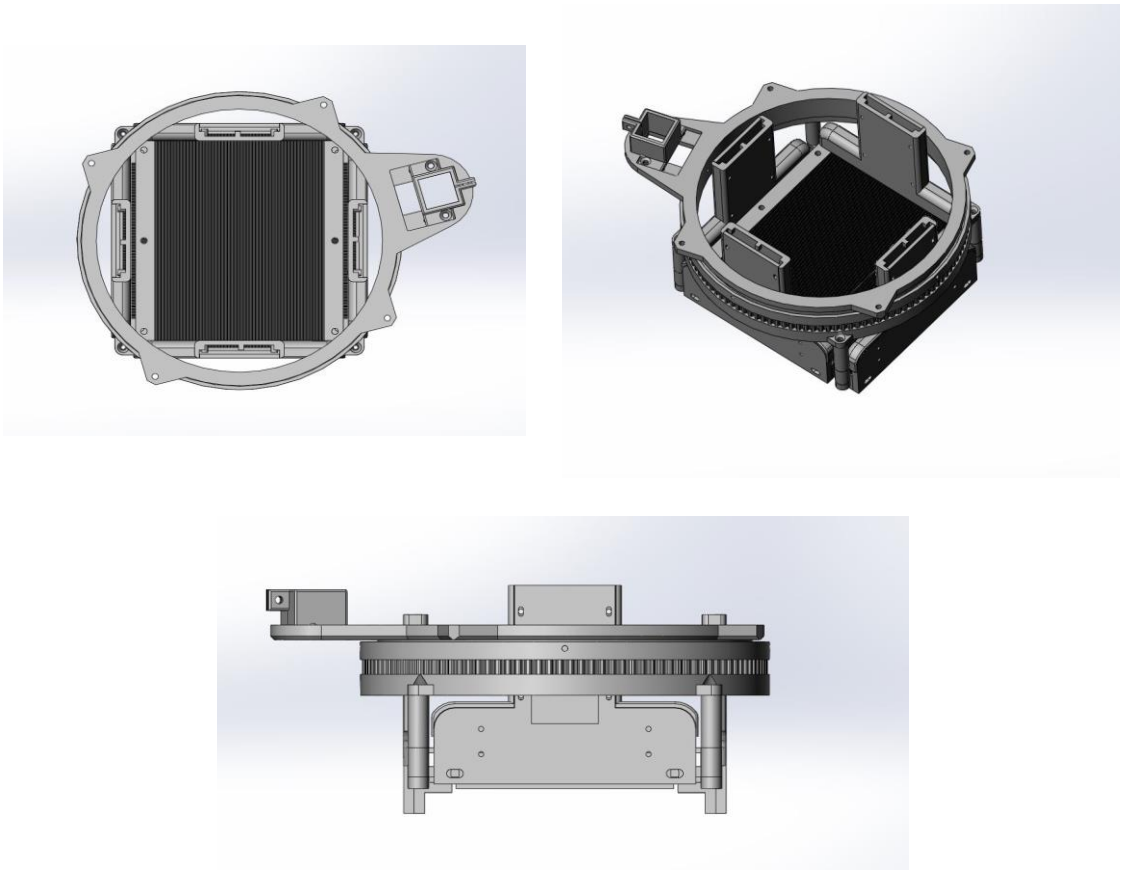

Figure 24. ***3D CAD Model of Detector Structure.*** This is the design of the detector in 3D CAD software.

To easily interface the detector with the linac, a typical accessory tray was modified so that it is possible to mount the detector to it. A large hole was milled out of the center of the accessory tray so that the radiation field produced by the linac would pass through it. This tray is then mounted directly to the linac head using the accessory tray mounting device.

Final considerations in the design include an electronics box so that the timing circuit could be securely fastened to the detector. This control box includes a fan to help regulate the temperature of the electronics and prevent them from

overheating. An indicator was also constructed so that, by visual inspection, it is possible to locate the angular position of the detector.

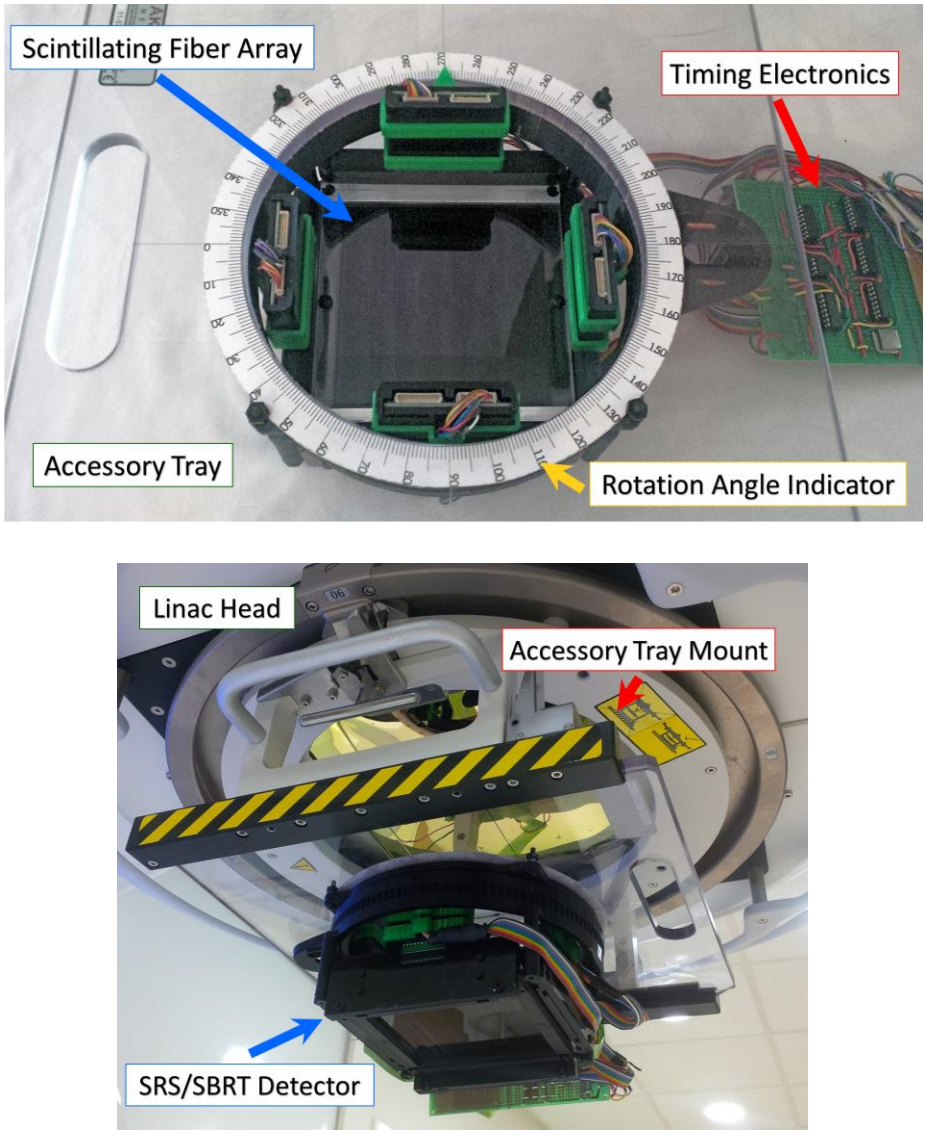

Figure 25. ***Mounting Detector to Linac.*** Top, photo of partially disassembled detector from above. Bottom, Photo of detector mounted on Elekta Versa HD linac.

c) Data acquisition

The final step in constructing a device capable of monitoring patient treatments was to create a data acquisition system. The hardware of the system is composed of a National Instruments PXI chassis with a fiber optic link to communicate with a computer outside of the linac vault. The PXI chassis includes a data acquisition board and also a motion input/output board. The data acquisition board is a National Instruments PXI-6255 multifuncion DAQ which supports up to 80 analog input channels with 16-bit resolution. The output from the driver circuit is connected to this board so that it can be processed using LabView software. The NEMA-8 stepper motor is connected to the motion input/output which is a National Instruments PXI-7340 motion controller. This allows the stepper motor to be controlled with the LabView motion software.

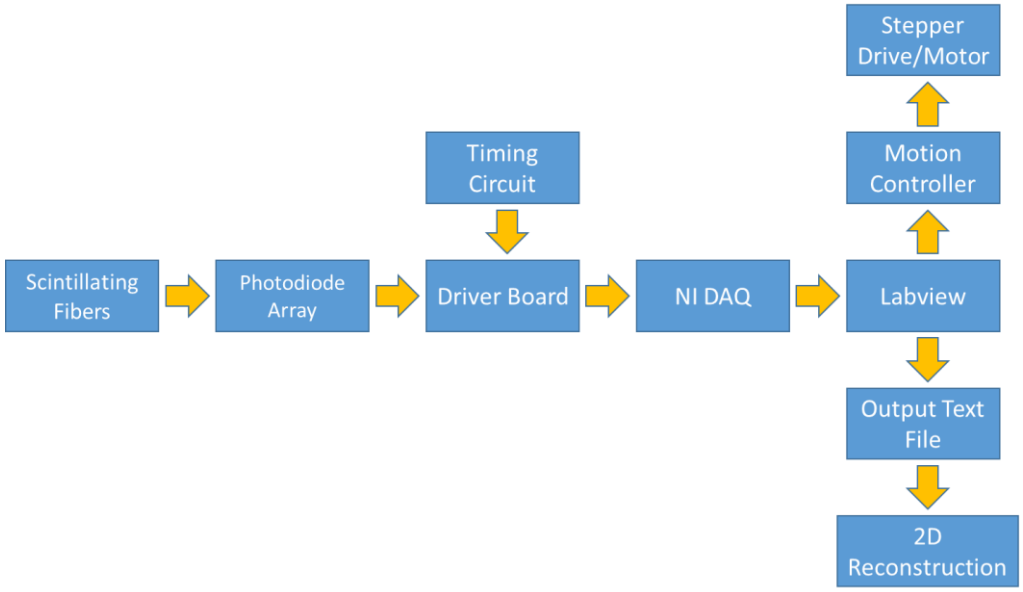

Figure 26. ***Block Diagram of Detector Operation.*** Block diagram showing basic detector function.

The LabView program was designed in-house and consists of a data acquisition loop which receives and stores the data from the detector and also integrates the motion of the detector. In the program, there are many parameters that the user can control including: input channels, number of samples, sampling frequency, number of samples to average, detector rotation speed, and number of degrees/steps to rotate.

B. Results

1) Calibration

A fiber array calibration is performed to eliminate variations in fiber and channel output due to slight differences in the coupling of each fiber to the

photodetector array and electronics. In addition, dosimetric calibration is performed with respect to the standard linac calibration field. The calibration, as a function of field size, was found to be quasi-constant from 3cm to 10cm. This process allows for a single dosimetric calibration factor to be applied to all the fibers of each array. The demonstration of non-constancy of the calibration factors for small fields is due to the output of the MLC for small fields. When comparing the output tables of the linear accelerator per field size to the change in calibration of the detector, we found that the same percentage difference occurs.

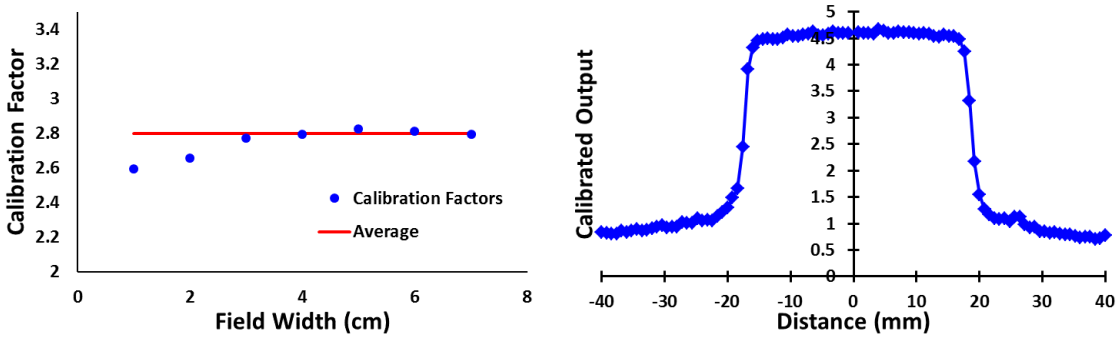

Figure 27. ***Fiber Calibration.*** The detector calibration is constant for field sizes greater than 2cm so a single calibration factor can be applied to the fibers for most clinically relevant field sizes. The figure at the left shows the calibration factors of a single fiber from a 1cm to 7cm field. The figure on the right shows the calibration factors of each fiber applied to a 5cm x5cm field.

Calibration was completed using field sizes from 1cm to 10cm in 1cm steps parallel to the fibers by delivering 100MU (100cGy at reference depth) and integrating every 8ms of linac pulses to reduce the variation in signal due to

fluctuating linac output. It was found that a different calibration factor set is required for each energy.

2) Dose rate independence

Detector response was tested as a function of dose rate from 100 MU/min to 600 MU/min for 6MV, 10MV, and 18MV photons. For all three energies, it was found that the detector system showed no significant change in detector response due to dose rate. This result indicates that there is no detector saturation nor missed pulses for each energy. Additionally, a test was performed utilizing flattening filter free fields.

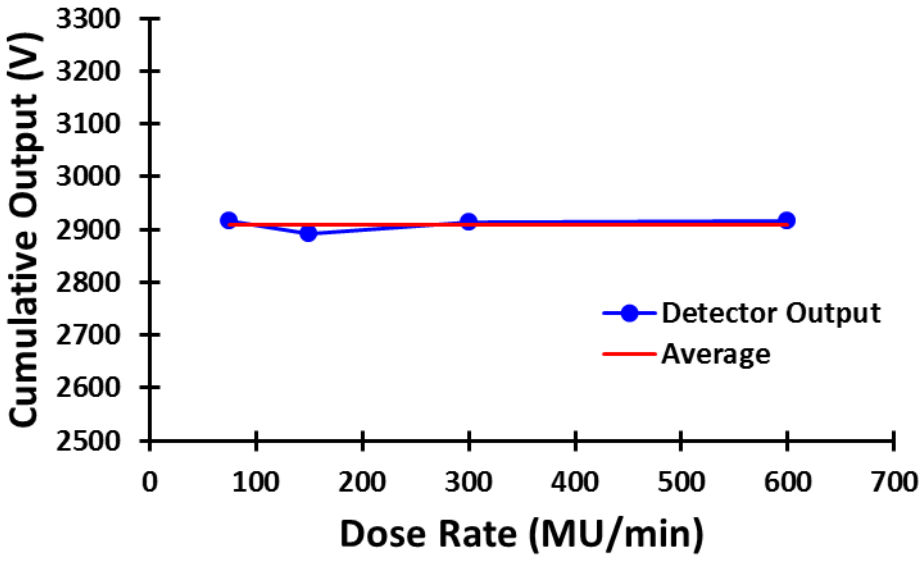

Figure 28. ***Dose Rate Independence.*** The field size was kept constant at 5cm along the length of all the fibers. 200MU were delivered at 75, 150, 300, and 600 MU/min and recorded with the detector system. This measurement was performed using three trials for each dose rate.

3) Longitudinal resolution

The response of the detector output was tested along the length of each fiber by varying the field size from 1cm to 10cm. The measurement was performed with the jaws and again with the MLC's. It was found that the response of the detector was linear with a linear correlation factor of 0.99. In addition, from 1cm to 2cm, the field was increased in 1mm increments which can be seen on the inset of the following figure.

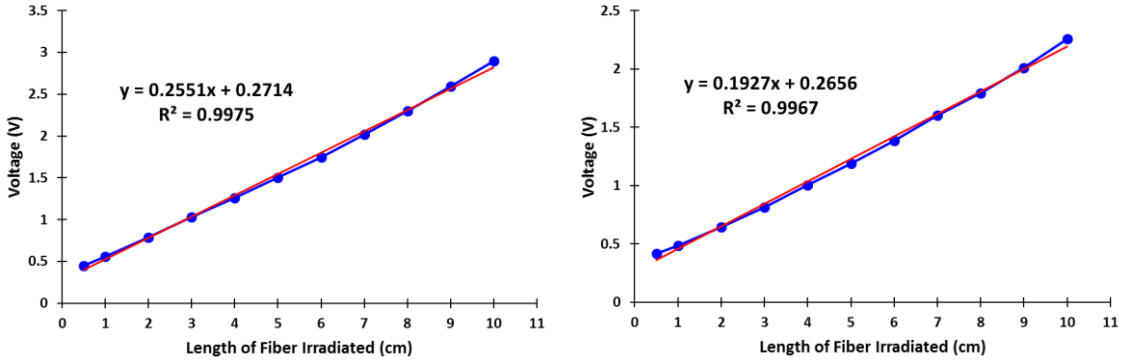

Figure 29. ***Spatial Linearity.*** Top, linearity response of detector when irradiated with 6MV photons. Bottom, linearity response of detector when irradiated with 18MV photons.

4) Lateral resolution

The field length along the fibers was set to a constant 5cm, and the field size perpendicular to the fibers was incremented from 5cm to 5.5cm by 1mm to test the detector's lateral resolution. The results show that there is minimal crosstalk between the fibers and that with interpolation the resolution of the

detector can be 0.1mm which is much better than the detector's intrinsic resolution of 0.8mm.

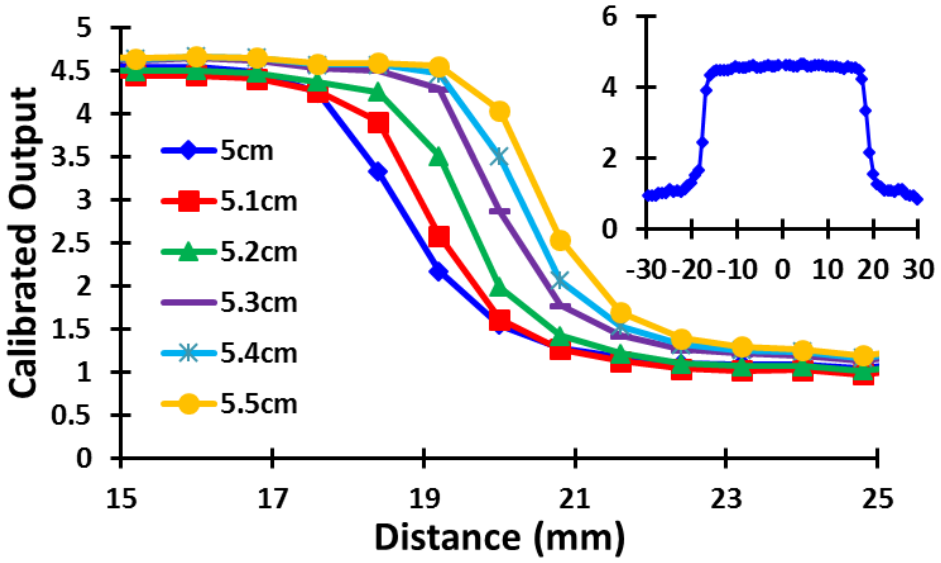

Figure 30. ***Lateral Resolution.*** A series of fields square fields 5cm x5cm to 5.5cm x5.5cm were delivered to the detector. The field size was incremented by 1mm to test the lateral resolution of the detector. The detector was cable of detecting each mm increment in field width. Note that the figure above is half of the field width therefore each 1mm increment in field size would increase half the field size by 0.5mm.

Typically, SBRT treatment fields are larger than 1 cm x 1cm, which is approaching the limit of the clinical MLC minimum field size. To test the ability of the detector to perform well under SBRT conditions, a 1cm x1cm field was created and 100 MU was delivered to the detector. The results of a measured dose profile are displayed in figure 31.

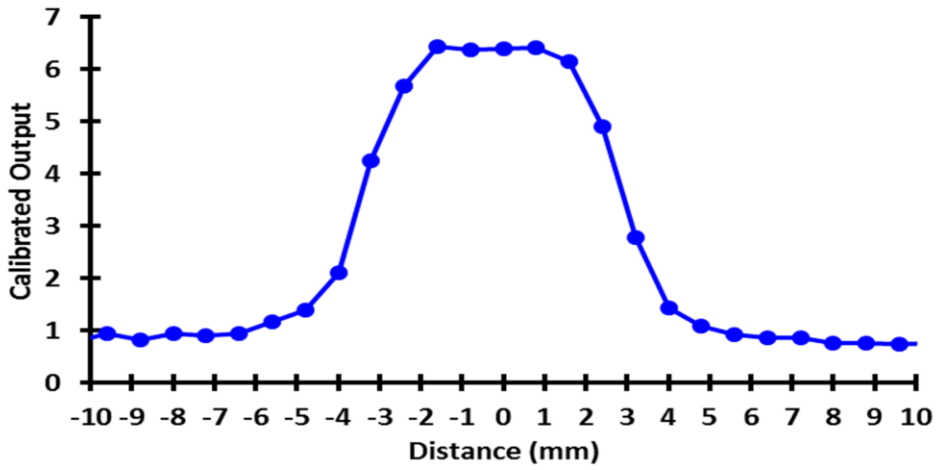

Figure 31 ***Small Field Profile.*** Figure showing a cross-section of a 1cm beam profile in the detector plane.

The detector was able to resolve the 1cm field with a large signal-to-background ratio. The data shows that further testing can continue with SRS cone fields smaller than 1cm.

5) Sensitivity

a) Dosimetric sensitivity

The dosimetric sensitivity was determined by using equation 4 from Chapter II. The average dosimetric sensitivity is 2075 mV/cGy and was calculated over the range of 10MU to 1000MU. The dosimetric sensitivity of the detector system exceeded expectations and can easily distinguish even a 1 MU discrepancy in treatment delivery.

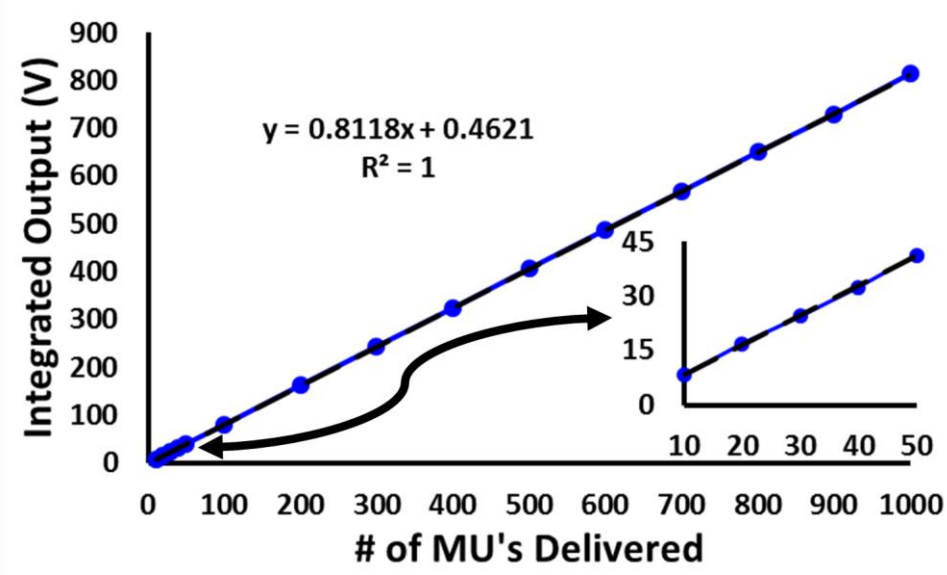

Figure 32. ***Dosimetric Linearity.*** Figure shows the linear output of the detector system vs. the number of monitor units (MU) delivered. Inset – Shows the linear response of the detector for every 10 MU delivered. The R^2 value is 1.

b) Spatial sensitivity

The spatial sensitivity was calculated using equation 3 from Chapter II. The average sensitivity of each fiber was determined for a single detector array using radiation field widths of 3cm, 4cm, and 5cm and delivering 200 MU for each field. Using a practical limit of 15mV for a confident measurement the spatial sensitivity of the detector system is 0.15mm along the fibers.

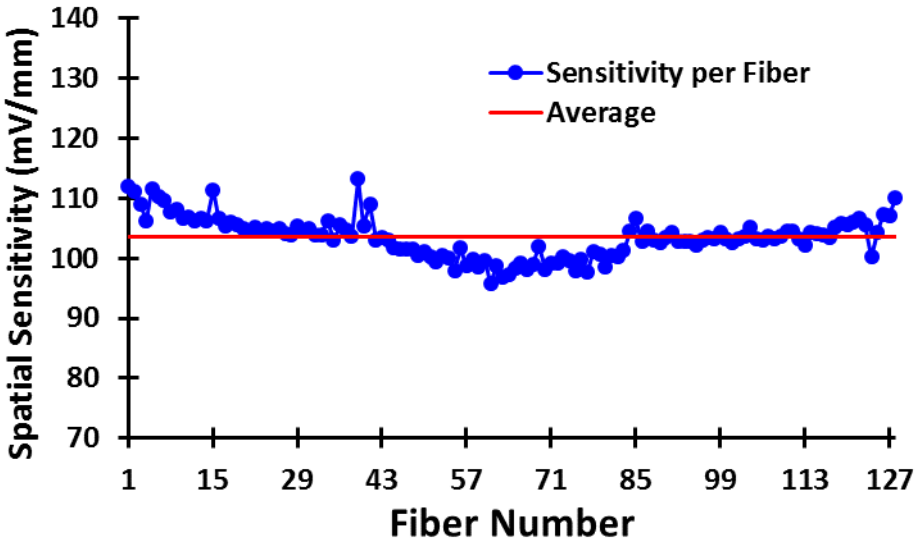

Figure 33. ***Spatial Sensitivity.*** The average spatial sensitivity of a single detector array per fiber for field widths of 3cm, 4cm and 5cm.

6) Time dependent output

To accurately monitor the dose delivered in real-time during patient treatment the detector must be able to display the current number of monitor units delivered. Since the detector integration is not synchronized with the linac output the detector will collect fewer pulses during one integration cycle and then collect more pulses during the next cycle creating a sinusoidal type output. Complicating things further, the linac output rate is not constant. However, as seen in the figure below the cumulative output is linear and its repeatability is very consistent.

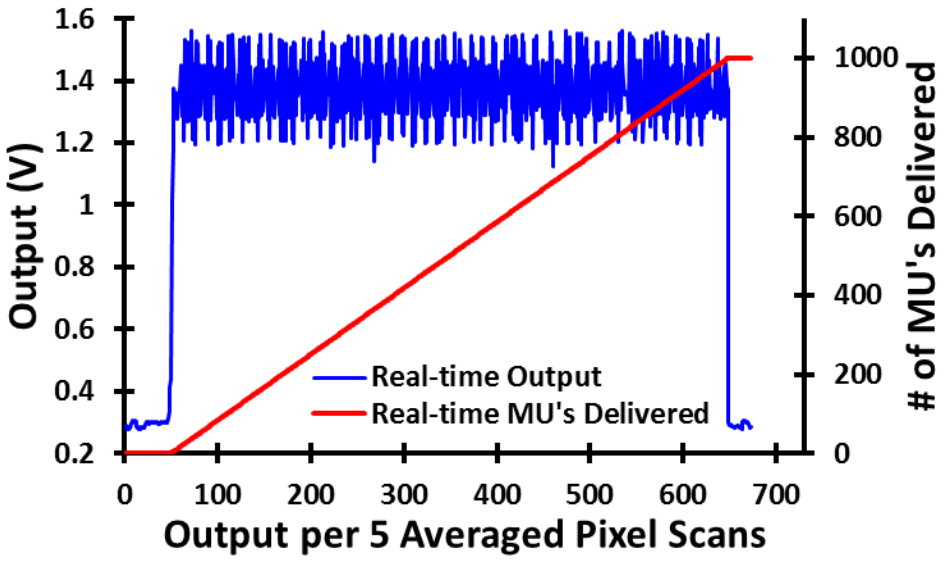

Figure 34. ***Time Dependent Output.*** Blue, shows the output of the detector system over time for a constant field size. Red, shows the cumulative output of the detector system over time. Each data point represents the averaged output for every 5 data sets (pixel scans).

7) Error detection

The main purpose of this detector is to catch errors before they become clinically significant during a treatment. To test the error detection capability of the detector a Rando Phantom was scanned using a clinical CT Simulator and imported into Pinnacle (treatment planning system). A typical spine SBRT plan was created using static IMRT radiation beams. The detector was then operated in static mode during the treatment delivery to the phantom. The figures below demonstrate the detectors response to the delivery of one beam which consisted of 5 control points and monitor units of 117MU for control point 1, 6MU for control point 2, 32MU for control point 3, 5MU control point 4, and 46MU control point 5. Each of the control points had significantly different field shapes to create a highly modulated field. A composite film

measurement was also taken at the treatment isocenter as a secondary validation that the detector output matched what was actually delivered by the machine.

The detector output shows excellent spatial agreement with the film measurement, as demonstrated in the following figure. However, the detector output is showing a response from leakage or scattering from the MLC. The scatter does not appear in the film because the film is located far enough away such that the leakage is scattered away from the treatment isocenter.

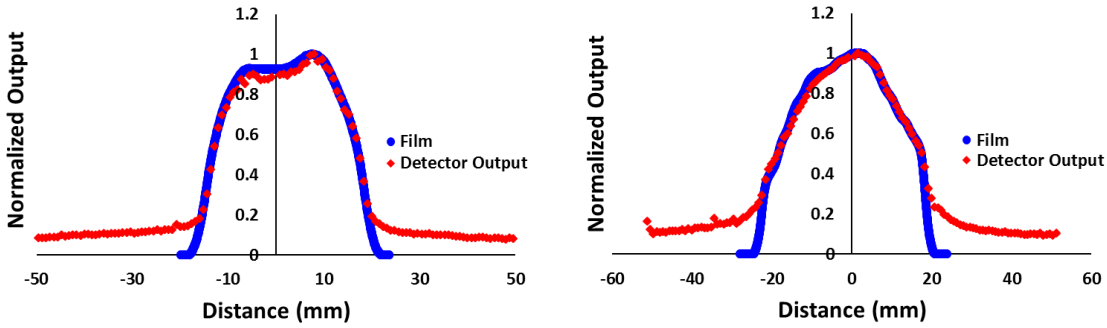

Figure 35. ***Composite Output at Isocenter.*** This figure displays the composite output from the detector while operating in static mode (red, diamond) compared to a film measurement at the linac isocenter (blue, circle). The figure on the left shows the profile along the MLC leaves and the figure on the right shows the profile along the jaws.

Another composite film measurement was performed with the film located on a plane as close as possible to the detector plane. The results show better agreement near the edges of the field where it is approaching background level. Additionally, the MLC output was exported from the treatment planning system so that a calculation of the expected output could be made for

comparison to the detector output. The results are displayed in the following figure.

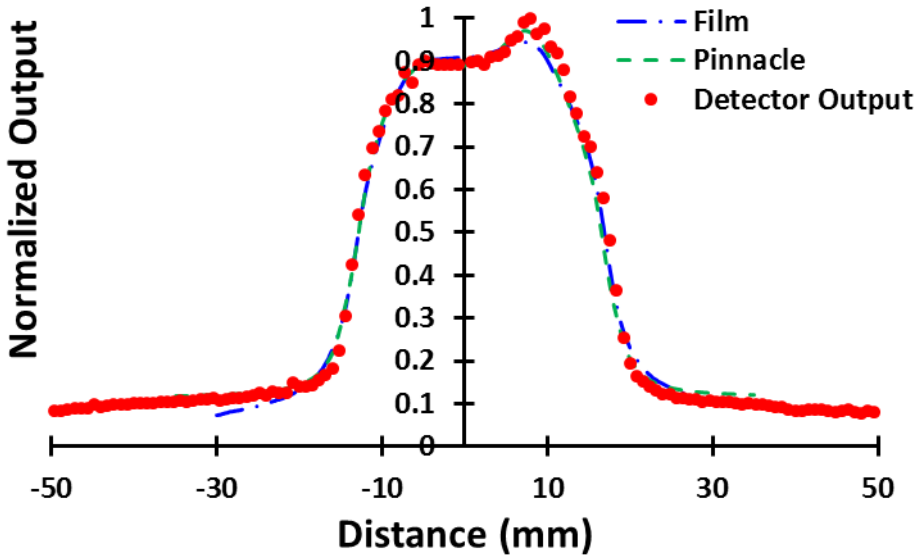

Figure 36. ***Composite Output at Detector Plane.*** Composite output with film on the same plane as the detector - A comparison between the film output, the detector output, and the planar dose exported from Pinnacle (TPS).

The results show that the detector output and the film measurements agree with the expected output. Clinical use of the detector is possible because the dosimetry team can export the expected fluence files from the TPS and when QA is ran with the detector the physics team can compare the results of the linac fluence with the planned fluence.

To perform a quick verification of the linac output the MLC position files can exported from the treatment planning system and an estimate of the delivered fluence can be calculated by multiplying the MLC leaf gaps by the number of

monitor units delivered. The following figure compares the detector output for the 5 controls points of the beam to the quick check described above.

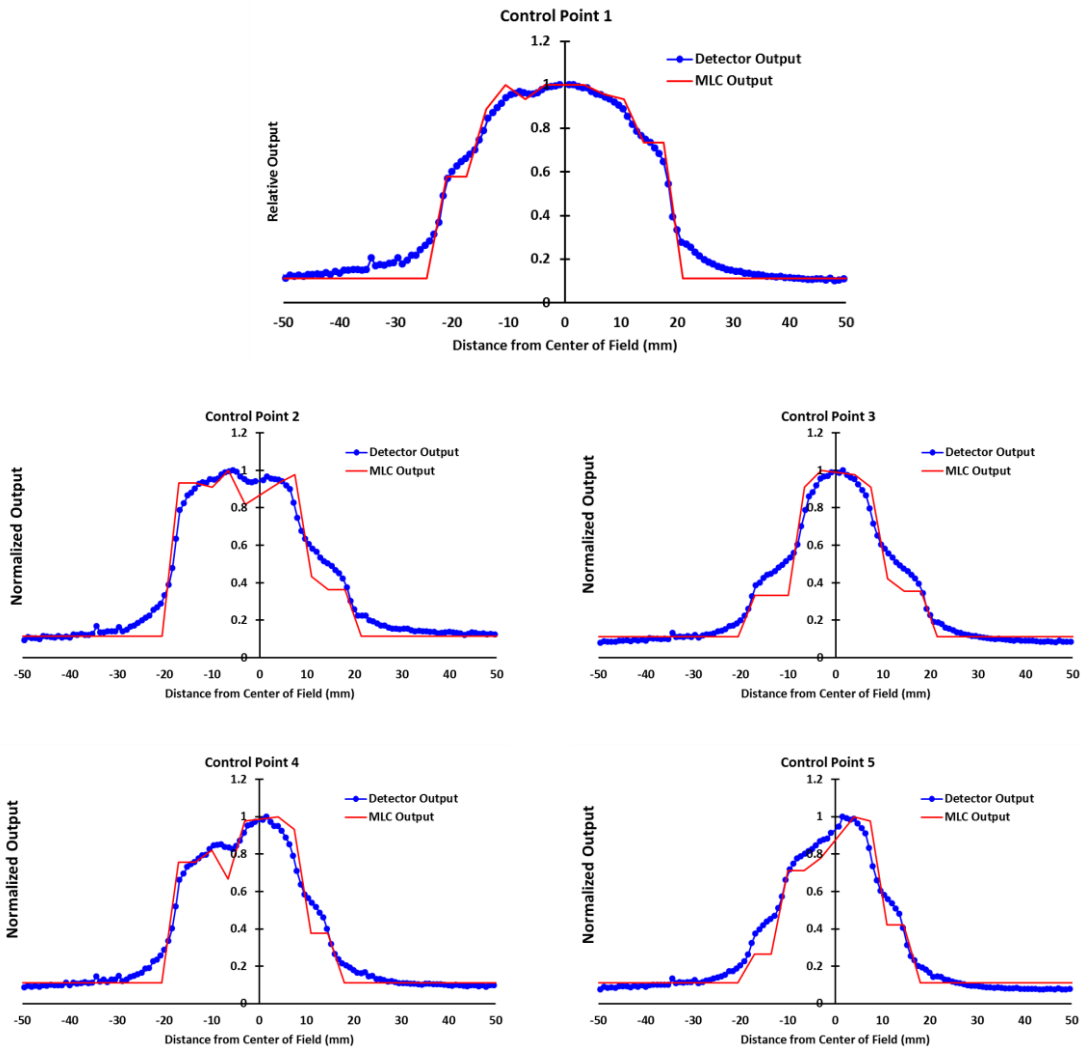

Figure 37. ***Detector Output Vs. TPS.*** The figure displays the output of the detector in static mode (blue) compared to the output sent to the MLC from the treatment planning system (red) for each control point in an SBRT static field.

Although, this test does not provide a high-resolution comparison between the expected output and the detector output it could be used as a quick first check to confirm that the linac is operating as expected.

8) Reconstruction

There are two main types of reconstruction methods: analytical reconstruction and iterative reconstruction. Analytical methods are typically more efficient and faster to compute than iterative methods, however they tend to produce more image artifacts such as streaks and noise. The most commonly used reconstruction technique until recent years has been the analytical filtered back projection method. This technique is a modification of the back-projection technique that applies a filter to reduce blurring. It has been used for many years in x-ray computed tomography (CT) reconstruction. Iterative reconstruction methods tend to be less efficient but are cable of reducing more image artifacts. Due to the advancement of computer processer and memory technology it has become possible to use more computationally intensive iterative reconstruction methods. The reconstruction algorithm chosen for the detector system is an iterative statistical reconstruction method developed in-house and is based off the maximum likelihood estimation method (MLEM). This method was chosen because it is proven to better handle artifacts than filtered back projection and provides higher spatial resolution.[23]

a) Number of projections:

Determining the minimum number of projections necessary to achieve a high-quality reconstruction is important to minimize computation time during

detector operation. Ideally, the detector should be able to take the necessary number of projections during critical moments of beam delivery and reconstruct the current beam profile. An example of a critical moment is a control point during a static beam for small IMRT fields. The minimum number of projections required for this detector setup was found to be 30 projections between 0 and 360 degrees. After acquiring 30 projections the increase in reconstruction accuracy is less than 0.1% from 30 to 360 projections. The results of this analysis can be seen in figure 38.

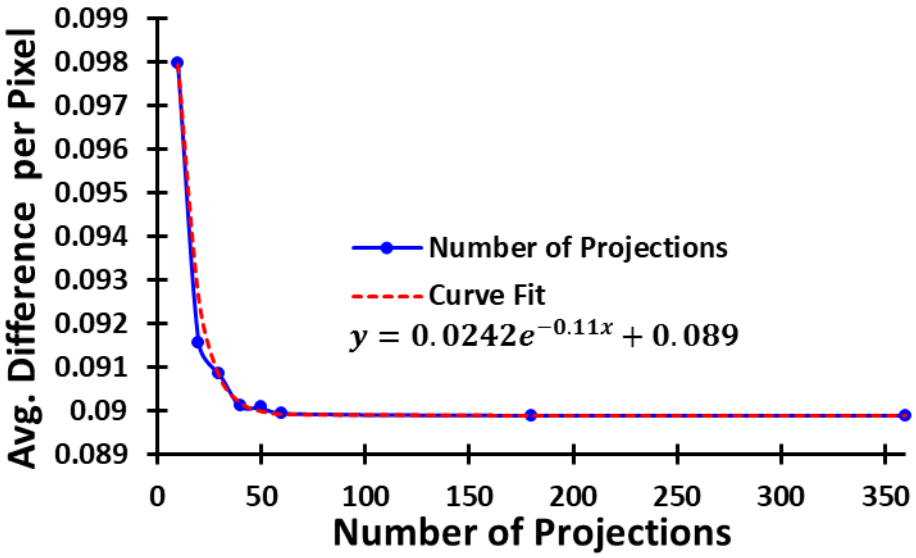

Figure 38. ***Ideal Number of Projections.*** The number of required projections required to provide a statistically insignificant increase in the accuracy of the reconstructed image is approximately 60 projections.

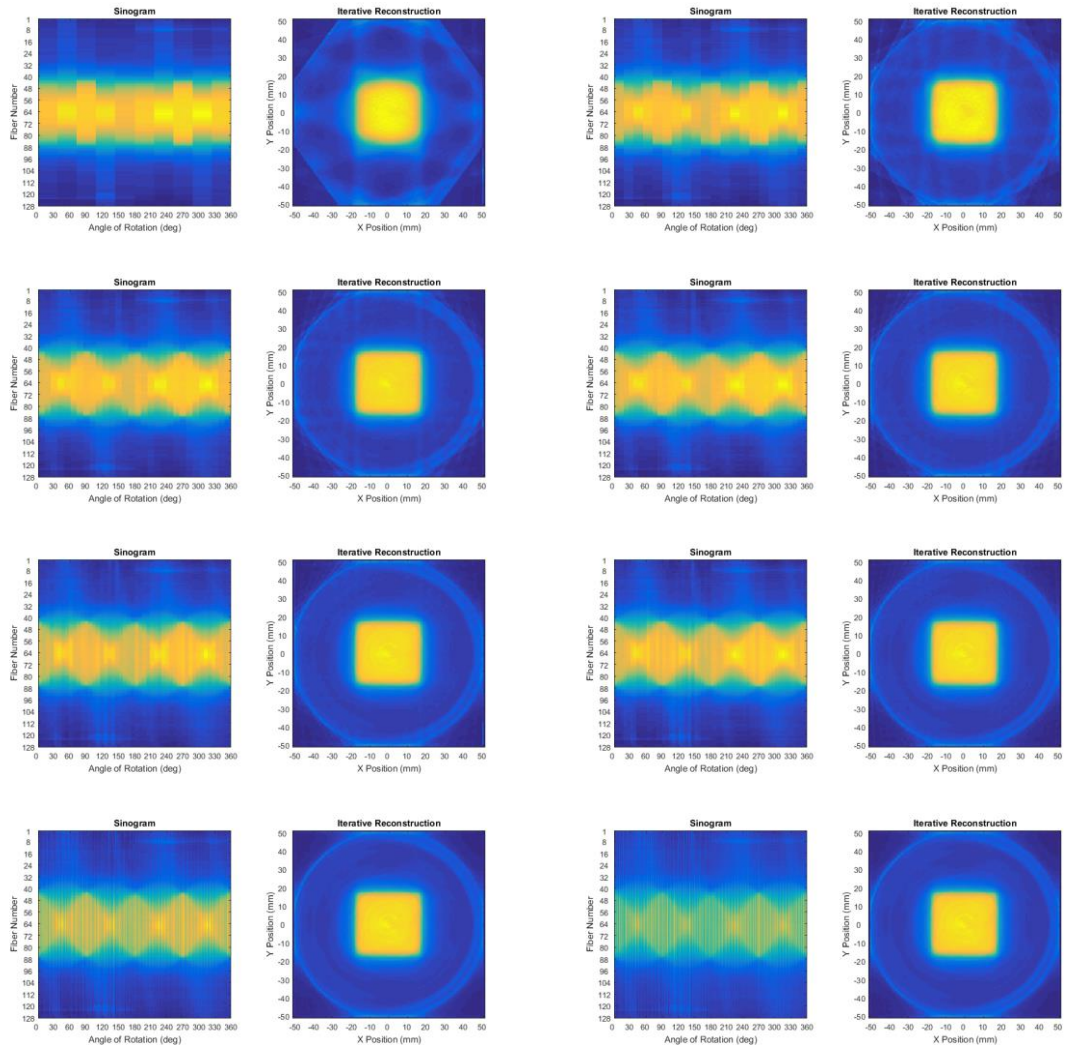

Figure 39. ***Minimum Number of Projections.*** There is a practical limit on the number of projections required to reconstruct a beam profile. Top left, 10 projections. Top right, 20 projections. Row 2 left, 30 projections. Row 2 right, 40 projections. Row 3 left, 50 projections. Row 3 right, 60 projections. Bottom left, 180 projections. Bottom right, 360 projections.

b) Reconstructed image resolution:

The output reconstruction image resolution is important to consider. The native resolution of the detector is 128 x 128 pixels. The higher the resolution of the output image the longer it takes for computations. Since the native resolution is already submillimeter, where 1 pixel = 0.8mm, using a resolution

of 128 x 128 pixels is reasonable because increasing the resolution will add more computation time and insignificant spatial information. However, a resolution of 256 x 256 pixels would be ideal and could be practical depending on the number of MU's being delivered for a critical phase of the treatment.

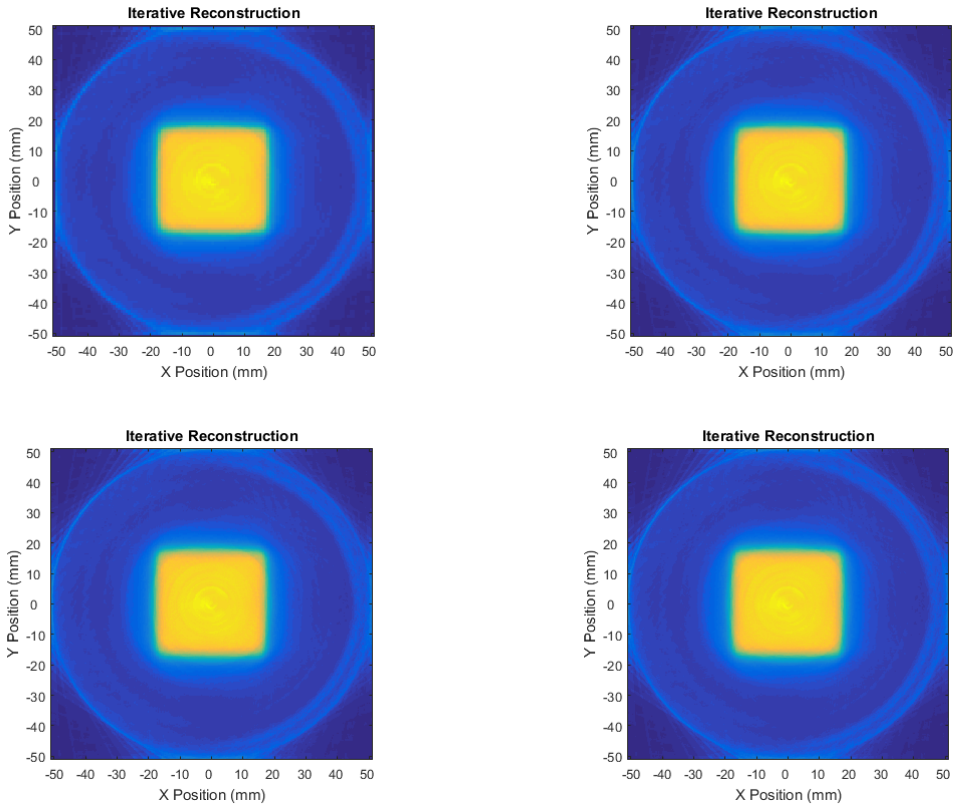

Figure 40. ***Resolution of Reconstruction Image.*** Top left, 128x128pixels. Top right, 256x256pixels. Bottom left, 512x512pixels. Bottom right, 1024x1024pixels.

c) Number of iterations:

Additionally, the number of iterations necessary to create an acceptable reconstruction image is critical. As the number of iterations increase the time required to create the reconstruction image also increases. The amount of time

required to reconstruct the images decreases significantly using parallel computing; however, it cannot always be assumed that every clinic will have a dedicated multi-core computer available. Fortunately, the number of reconstruction iterations greater than 25 do not add significant increases in the quality of the output image. In fact, the reduction in reconstruction error does not change more than 0.1% from 25 to 60 iterations. Using a 3.2Ghz Quadcore CPU and 16Gb of RAM the reconstruction algorithm takes less than 0.5 seconds to perform 25 iterations with an output image resolution of 128x128 pixels.

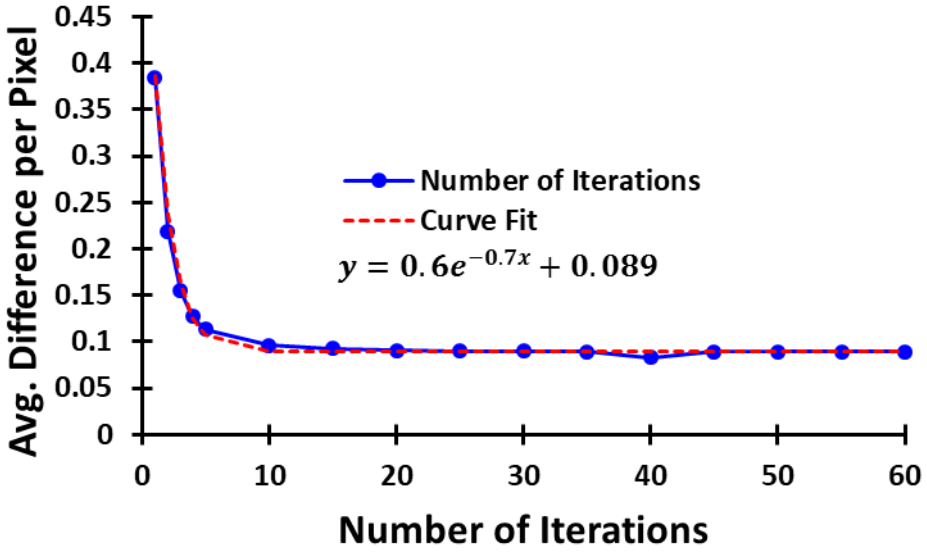

Figure 41. ***Number of Iterations Required.*** The number of iterations required to provide statistically insignificant change in the accuracy of the reconstruction image is approximately 10.

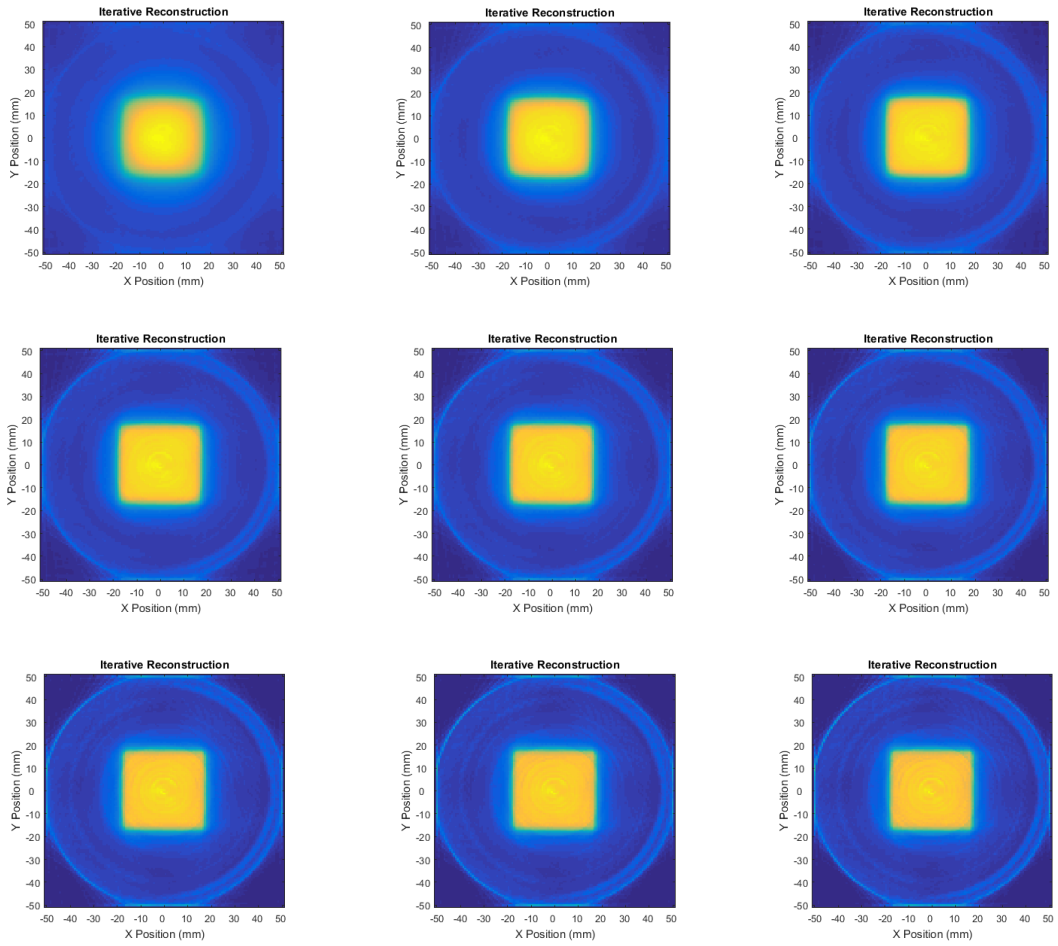

Figure 42. ***Number of Iterations.*** Top left, 5 iterations. Top middle, 10 iterations. Top right, 15 iterations. Row 2 left, 20 iterations. Row 2 middle, 25 iterations. Row 2, right, 30 iterations. Bottom left, 40 iterations. Bottom middle, 50 iterations. Bottom right, 60 iterations.

d) Detector rotation speed

An important consideration when designing a detector that reconstructs beam profiles through rotation of a detector array is the maximum speed of rotation. The maximum speed is defined here as the maximum speed that the detector can rotate without causing significant loss in the reconstructed image quality. The quality of the reconstruction image is based on more than just the number

of projections taken during the rotation. Since each detector array is read in a sequence, there is a small time delay of 8 milliseconds between each data set. As the detector rotates, it causes a time delay between the known position of the detector and the output data. To find the maximum useful rotation speed of the detector, a 5cm x5cm 6MV beam was reconstructed using a 180-degree rotation speed of 0.5, 1, 2, 3, and 4 seconds.

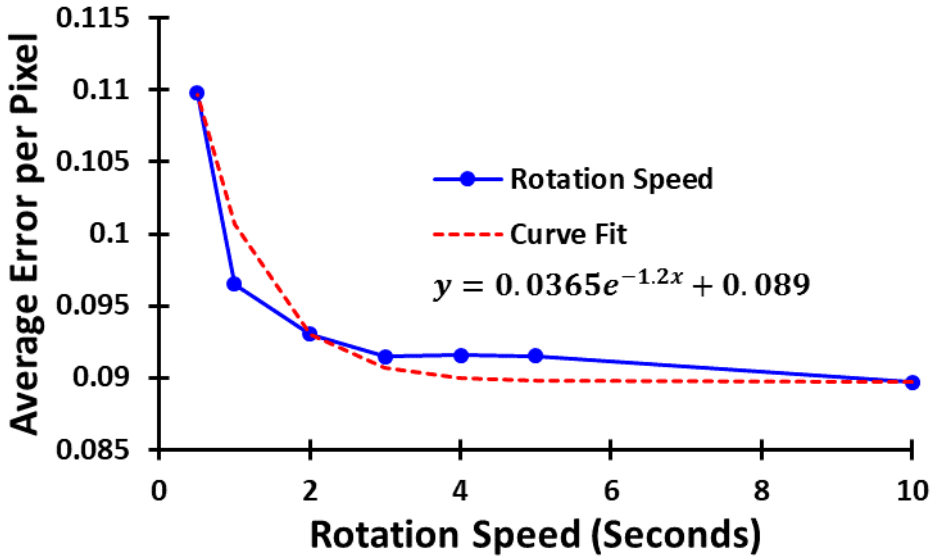

Figure 43. ***Detector Rotation Speed.*** The detector rotation speed required to accurately reconstruct the image is approximately 3 seconds.

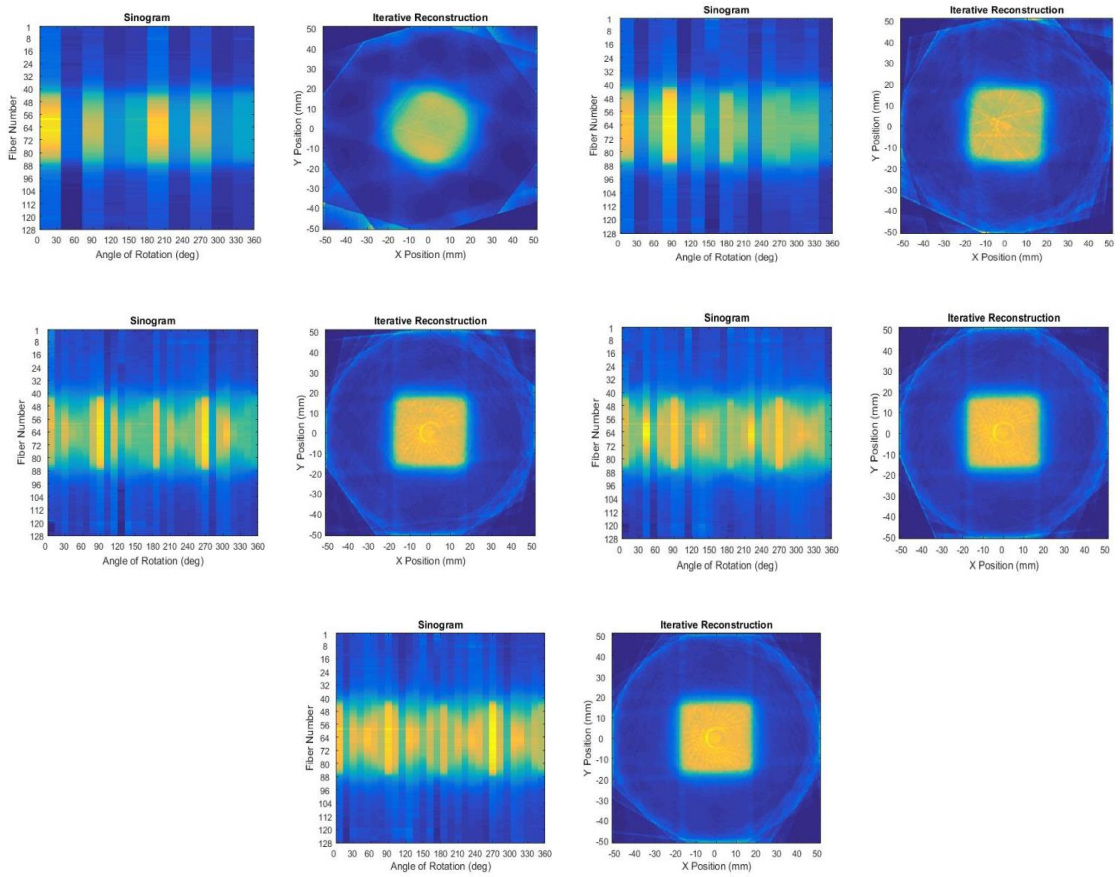

Figure 44. ***Rotation Speed.*** This figure displays the results of the rotation speed test from 0 to 180 degrees. Top left, 0.5 second rotation speed. Top right, 1 second rotation speed. Middle left, 2 second rotation speed. Middle right, 3 second rotation speed. Bottom, 4 second rotation speed.

From the data, the maximum 180-degree rotation speed without a correction is 2 seconds. A maximum rotation speed of 2 seconds is adequate for most static fields because the number of monitor units delivered in a typical static beam is greater than 20 monitor units at a dose rate of 600 MU/min. However, with an angular correction factor, it is possible to reduce the speed of the detector rotation to 1 second. The master clock speed of the detector system can also be increased up to 4 times the current 1Mhz frequency which will also greatly reduce the rotation speed of the detector by increasing the number of

output data sets per second. The reduction in error with a decrease in rotation speed is 0.4% when changing the rotation speed from 2 to 10 seconds.

e) Complex field reconstruction

In the previous sections the detector has been shown to reconstruct a simple square field, however most treatment fields are not simple shapes that are easily reconstructed. To test that the detector is capable of more complex reconstructions a series of more difficult fields were delivered to the detector. The first being a trident type field. The trident shape is useful because it has very deep concavities. In many static beam deliveries, there are multiple control points for each field. Each of these control points are designed to modulate the beam fluence so that the desired dose is delivered to the target and surrounding tissues are spared and, typically, there a few control points in each treatment field with deep concavities.

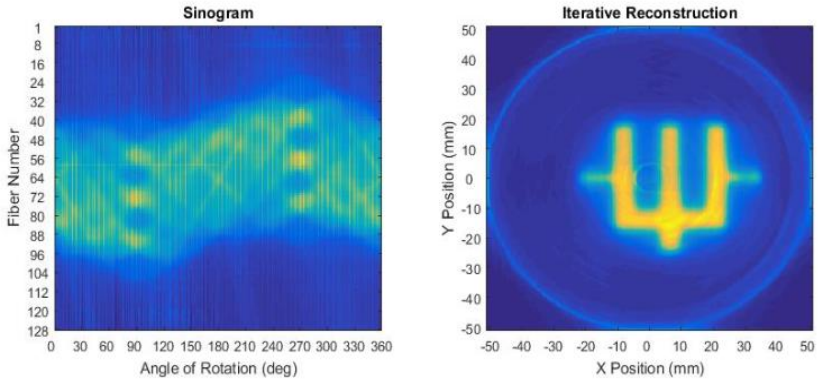

Figure 45. ***Concave Reconstruction.*** A trident field shape was reconstructed to demonstrate that the detector system can reconstruct profiles with deep concavities.

As shown in the figure above the detector could reconstruct the trident shape accurately. In addition, the field was purposely offset from the detector center so that we could test for any artifacts that might appear from a non-symmetrical reconstruction. Interestingly, the detector performed better than expected because the leakage between the MLC leaves can be seen near the edges of the field. This is present because the jaws were not covering the leaves near the edge of the field. These leaves are considered closed to the machine but there is still a small 5mm gap between the leaves. This finding is important because it is possible to monitor the jaw position and detect whether the jaws are allowing non-desired extra leakage through the MLC leaves.

The detector also needs to be able to reconstruct beam profiles that may not be a continuous open field. For instance, the MLC leaves may be modulating the beam in such a way that there are three distinct beamlets within one treatment field. To test this, a field was created with three separate openings in the

MLC's with distinct shapes. As shown in the figure below, the detector was capable of accurately reconstructing the field and again we can see that the detector was also capable of detecting the leakage from between the closed MLC leaves.

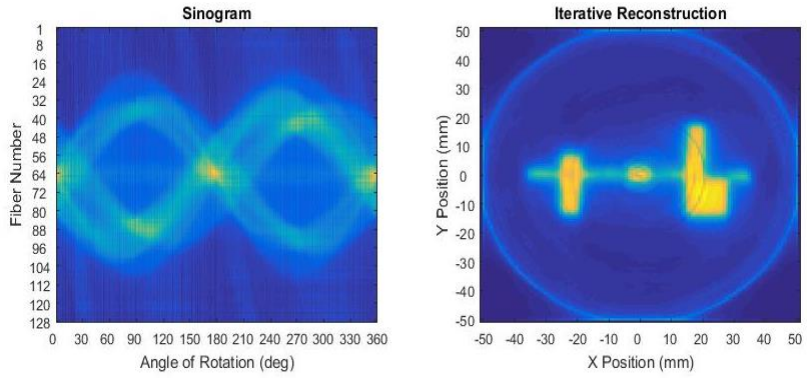

Figure 46. ***Multiple Beamlets in a Single Field.*** This figure displays the detector's capability of reconstructing a beam profile with several beamlets.

f) Artifact reduction:

Initially, the reconstruction algorithm used was a modified version of the Fessler package that is available for academic use and compiled using MATLAB. The code was modified slightly to better suit the needs of this detector since the code was typically used for computed tomography and gamma camera image reconstruction. Due to some small defects in the construction of the fiber arrays there is often a ring artifact and occasionally a photodiode stops functioning properly. Two different methods were tested to

reduce the artifact in the image. The first using the modified Fessler version of the algorithm and using the sliding averaging function in MATLAB to average the neighbors of each pixel in the sinogram but only averaging between the pixels in each projection. This method worked quite well in reducing any artifacts in the image, however at the cost of resolution in the output image. The second method is averaging to the nearest pixels around a bad pixel. To decide which pixel needs to be fixed in the code, a threshold was applied so that if any pixel was very different from its neighbor the code replaces that pixel with the average between its neighbors. The following figure displays the difference between a raw reconstruction image and a smoothed sinogram reconstruction using the sliding window averaging technique with the modified Fessler package. This smoothing function eliminated the artifact but the image has been blurred slightly.

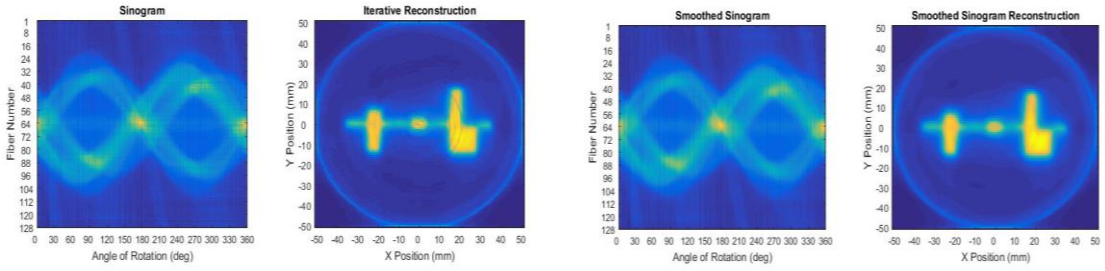

Figure 47. ***Artifact Reduction.*** Figure comparing reconstruction methods using MATLAB. Left, 2D reconstruction performed without any smoothing operations. Right, 2D reconstruction with threshold smoothing. The sinograms are reconstructed using 30 iterations and 256x256 pixel output image. The smoothed sinogram is generated using a threshold of 95%.

The figure above depicts the efficacy of the threshold nearest neighbor technique. The artifact is not completely eliminated; however, the effect of the artifact is reduced and the resolution of the image remains mostly unchanged.

g) Development of in-house C code

To have a better understanding of the MLEM algorithm, reduce image artifacts, and decrease the computation time an in-house developed algorithm was written in the C programming language.

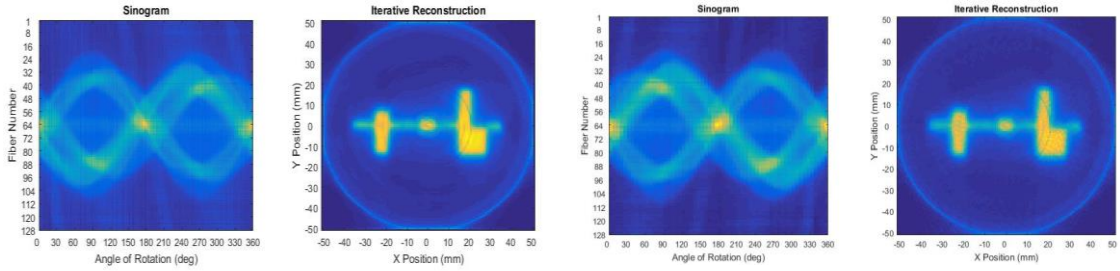

Figure 48. ***C code Vs. MATLAB Reconstruction.*** Left, 2D reconstruction using an in-house developed C code. Right, 2D reconstruction using the MATLAB code. Both reconstructions are performed using 30 iterations with an image resolution of 256x256pixels.

The figure above demonstrates the in-house developed MLEM code. The difference between the output of the two codes is minimal, however, having a code that is fully understood is advantageous. Further development of the code is now possible without complications of unknown syntax and functions.

h) Reconstructed profile error detection

The same SBRT spine treatment delivered in section 7 was delivered to the detector in rotation mode. To test the capability of the system's detection of MLC errors, another field was created in the treatment planning system by adjusting the MLC positions of the correct field so that they simulate errors. The first test was done by displacing the MLC at random from 1mm to 5mm in one bank of MLC leaves. Both the correct (normal) beam and the beam with MLC "errors" were delivered to the detector. The data was collected and exported from the LabVIEW program and reconstructed. The reconstructed fields were then imported into the RIT film QA software. The two fields were registered together using the center of the field and a gamma test was performed to compare the two treatment fields using the criteria of 1%, 1mm. From the analysis, the detector could resolve the errors in MLC leaf placement. The results of the test are displayed in the following figure. It is important to note that there was no auto registration performed when using the gamma analysis. This shows that the fields reconstructed by the detector are reproducible and accurate.

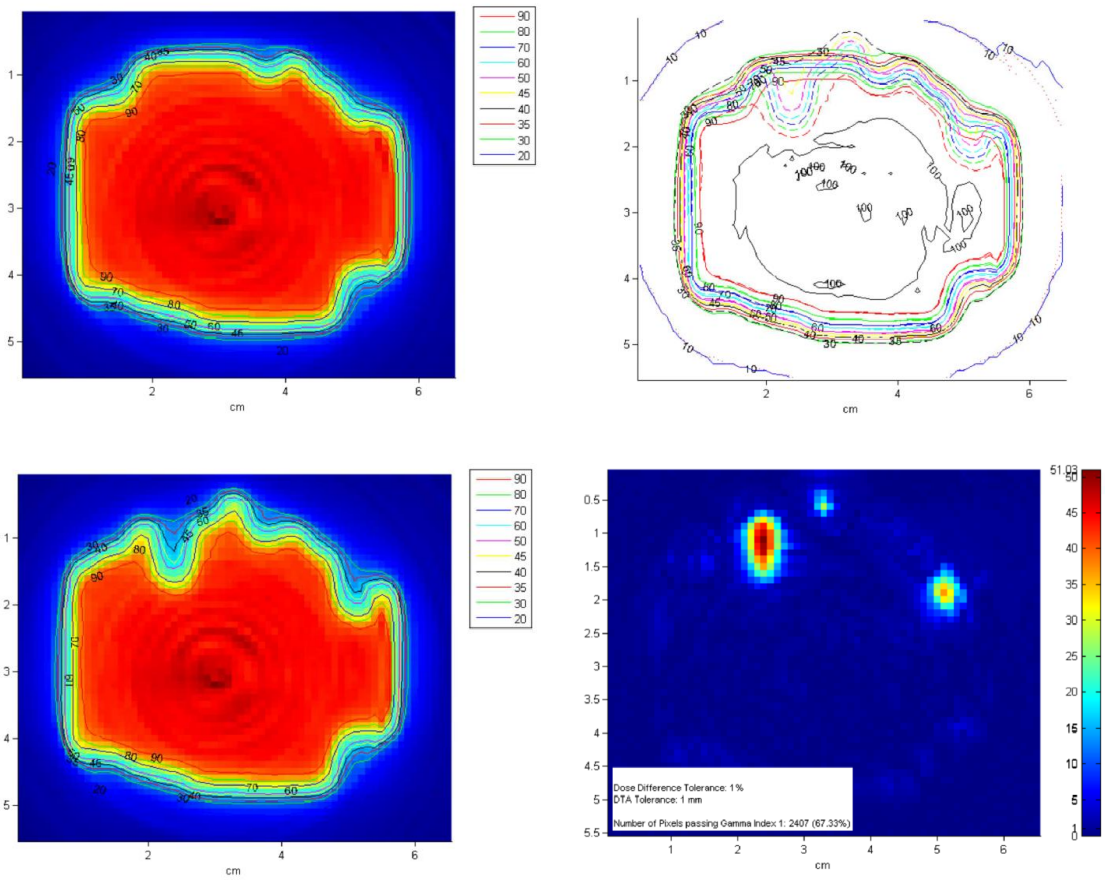

Figure 49. ***Random MLC Errors.*** Two SBRT spine fields were delivered to the detector system. The first was a correct field (top left) containing no errors and the second field contained induced MLC errors (bottom left). Both fields were reconstructed using the in-house developed code. The system could detect the MLC leaves that were in the wrong position. This is clearly visible when the isodose lines are overlaid (top right). A gamma analysis was then performed using the criteria of 1%, 1mm (bottom right). The gamma test clearly shows the error in the MLC positions.

Another test was performed using the same correct, "normal", field and another field that contained only a single MLC leaf displaced by 1mm inside the field. Like the first test, the data was reconstructed and imported into the RIT film QA software. A gamma test comparing the two fields was performed using the criteria of 1%, 1mm. Again, the detector could resolve the displaced MLC leaf. The results are shown in the following figure.

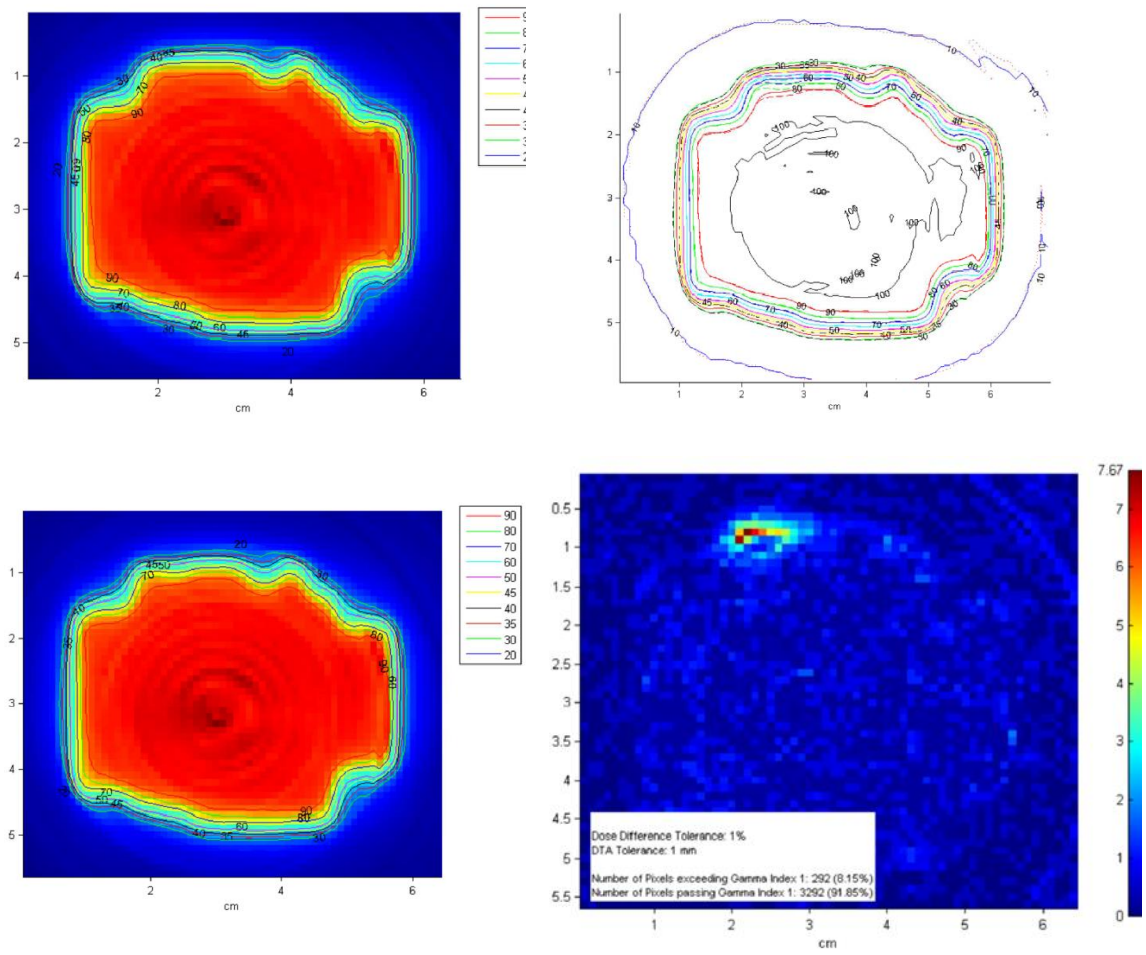

Figure 50. ***1mm MLC Leaf Error.*** Two SBRT spine fields were delivered to the detector system. The first was a correct field (top left) containing no errors and the second field contained an induced 1mm MLC error (bottom left). Both fields were reconstructed using the in-house developed code. The system could detect the MLC leaves that were in the wrong position. This is clearly visible when the isodose lines are overlaid (top right). A gamma analysis was then performed using the criteria of 1%, 1mm (bottom right). The gamma test clearly shows the error in the MLC position.

C. Analysis and discussion

The detector system is based on two orthogonal high-resolution scintillating fiber arrays with photodiodes coupled to each end of the scintillating fibers. The arrays are mounted to a rotation system to rotate the arrays 180 degrees to measure 360 degrees of projections. The fibers are embedded within a

substrate to create a water equivalent and homogenous detector plane. The structural materials are made from 3D printed material to limit the scatter of ionization radiation. The detector was designed with these characteristics so that it could be operated in transmission mode during a patient's treatment. The detector system is developed with high-speed processing and data acquisition electronics to monitor the output of the linac in real-time in-vivo. The detector snaps into the standard accessory tray mount provided by the linac manufacturer allowing for quick and easy setup.

With a minimum number of 30 projections, minimum rotation speed of 2 seconds, and a nominal linac dose rate of 600MU/min of 6MV photons the detector is capable of reconstructing beamlets as small as 20MU, which corresponds to 0.67MU per projection. Using 30 iterations of the reconstruction algorithm a field can be reconstructed in less than 0.5 seconds.

The detector was validated using varying ionizing radiation field sizes, output, photon energy and dose rates. Tests included the verification of the detector linear response to change in field size and linac output for parameters typical of SBRT and SRS treatments. The system can determine a 1cGy change in output and submillimeter changes in MLC leaf positioning with minimal crosstalk between fibers. With an integration time of 8ms and a total output time of less than 50ms the detector is capable of real-time error detection.

The data presented shows that 2d reconstruction of the beam profile is possible using a minimum of 30 projections with a rotation speed as low as 2 seconds without corrections and 25 reconstruction iterations. Although the detector is an integrating type detector that is not synchronized with the linac, the detector is sensitive and fast enough to reconstruct each control point of a static SBRT field.

IV. GENERAL CONCLUSIONS

We have validated the development of the first two in-vivo, real-time, high-resolution transmission detectors for linac based patient QA. Each system is a compact and high-speed detector with scintillating fibers coupled directly to front-end photodiodes to create low cost monolithic detector elements. In addition, the systems are Cherenkov radiation corrected using spectral filtering to produce high-density arrays with very low noise which makes high-speed detection feasible.

We demonstrated the feasibility of the proposed detector to capture deviations from treatment errors and general tests of technology fundamental operational parameters to provide real-time transmission detection of external beam radiotherapy. We anticipate that this detector technology will improve treatment verification and patient safety which will lead to an enhanced cancer treatments.

Reported results of our novel detector architectures based on scintillating fiber arrays show that their sensitivity will surpass current limitations in detecting real-time linac output present in other technologies. Furthermore, its implementation in clinical operations will achieve a higher standard of patient safety and dose delivery accuracy. We demonstrated that the developed detectors are the first of their kind to accurately detect the linac output with

high-resolution when only a fraction of the typical dose has been delivered without noticeable false positives. The detectors can monitor a single output pulse from the linac and have the sensitivity to analyze MLC leakage. This work also established the practical number of projections, iterations and rotational speed required to perform 2D reconstruction utilizing scintillator fiber arrays with minimal error. In addition, the first tests were performed for the determination of lateral resolution in fiber scintillators. For the first time therapists and physicist can perform 2D reconstruction and visualize the treatment fields in real-time while delivering radiation to a patient. The detectors will set a new benchmark for spatial resolution and dosimetric sensitivity of external beam QA instruments.

We would like to emphasize the overall purpose of developing the reported real-time dosimeter is to improve the current practice of external beam cancer treatment towards the enhancement of treatment efficacy and patient safety. The scintillating fiber technology reported in this work will be the central instrument to achieve this goal. The data reported has validated the development of the hardware for real-time imaging dosimeters using scintillating fiber arrays to improve external beam treatment accuracy and safety which will benefit the large number of cancer patients currently treated with external beam radiotherapy.

V. REFERENCES

1. *IQM: Integral Quality Monitor*. iRT Systems GmbH, 2014.
2. *Dolphin Patient QA and Monitoring*. IBA, 2016.
3. *Delta4 Discover: Measure the Dose to the Patient at Treatment*. ScandiDos.
4. Knoll GF. *Radiation detection and measurement.* 4. ed. ed. New York [u.a.]: Wiley; 2010.
5. Horrocks D. *Organic Scintillators and Liquid Scintillation Counting: Proceedings of the International Conference On Organic Scintillators and Liquid Scintillation Counting, University of California, San Francisco, July 7-10, 1970.* Academic Press; 2012.
6. *Scintillating-Optical-Fibers*. Saint-Gobain Ceramics & Plastics, Inc., 2005-2017.
7. Archambault L, Beddar AS, Gingras L, Lacroix F, Roy R, Beaulieu L. Water-equivalent dosimeter array for small-field external beam radiotherapy. *Medical Physics.* 2007;34(5):1583-1592.
8. Beaulieu L, Beddar A, Lacroix F, Archambault L, Gingras L, Guillot M. Clinical prototype of a plastic water-equivalent scintillating fiber dosimeter array for QA applications. *Medical Physics.* 2008;35(8):3682-3690.

9. Frelin AM, Fontbonne JM, Ban G, et al. Spectral discrimination of Čerenkov radiation in scintillating dosimeters. *Medical Physics.* 2005;32(9):3000-3006.

10. Attix FH. *Introduction to radiological physics and radiation dosimetry.* Weinheim [u.a.]: VCH; 2007.

11. Hagopian V. Optical fibers light yield and radiation damage. *Nuclear Physics B (Proceedings Supplements).* 1998;61(3):355-359.

12. Bongsoo L, Kyoung Won J, Wook Jae Y, et al. Measurements of Cerenkov Lights Using Optical Fibers. *IEEE Transactions on Nuclear Science.* 2013;60(2):932-936.

13. Law SH, Suchowerska N, McKenzie DR, Fleming SC, Lin T. Transmission of Čerenkov radiation in optical fibers. *Optics Letters.* 2007;32(10):1205.

14. Wiles A, Rangaraj D, Loyalka S, Izaguirre E. TH-C-17A-08: Monte Carlo Based Design of Efficient Scintillating Fiber Dosimeters. *Medical Physics.* 2014;41(6Part32):555.

15. Liu PZY, Suchowerska N, Abolfathi P, McKenzie DR. Real-time scintillation array dosimetry for radiotherapy: The advantages of photomultiplier detectors. *Medical Physics.* 2012;39(4):1688-1695.

16. Janesick JR. *Scientific charge coupled devices.* Vol 83. Bellingham, Wash: SPIE Press; 2001.

17. SFH 229/SFH 229 FA: Silicon PIN Photodiode with Very Short Switching Time. OSRAM, 2001.

18. AD8065/AD8066: High Performance, 145 MHz FasFET Op Amps. Analog Devices, 2002-2016.

19. *AD7606/AD7606-6/AD7606-4: 8-/6-/4-Channel DAS with 16-Bit, Bipolar Input, Simultaneous Sampling ADC.* Analog Devices, 2010-2017.

20. Van Dyk J, Smathers JB. The Modern Technology of Radiation Oncology: A Compendium for Medical Physicists and Radiation Oncologists. In. Vol 27: American Association of Physicists in Medicine; 2000:626-627.

21. Khan FM. *Physics of Radiation Therapy.* 4 ed. Philadelphia: Wolters Kluwer Health; 2009.

22. Klein EE, Hanley J, Bayouth J, et al. Task Group 142 report: quality assurance of medical accelerators. *Med Phys.* 2009;36(9):4197-4212.

23. Wieczorek H. The image quality of FBP and MLEM reconstruction. *Physics in Medicine and Biology.* 2010;55(11):3161.

VI. VITA

Tyler Knewtson was born in Joplin, MO to Kelly and Dana Knewtson. He attended and graduated from Joplin High School, Magna Cum Laude. After receiving his diploma, he continued his studies at Missouri University of Science and Technology where he obtained a Bachelor of Science in Nuclear Engineering, Magna Cum Laude. Concurrently, he earned a nuclear reactor operator license at the research reactor and was active in several honor societies. He then accomplished a Master of Science in Nuclear Engineering with an emphasis in Medical Physics at the University of Missouri. He worked on eye-plaque brachytherapy research with Washington University in St. Louis and became interested is applying Nuclear physics to medical applications as a master student. He remained at University of Missouri for his doctorate. As a Ph.D. candidate, he has worked at Scott and White in Temple, Texas and University of Tennessee as a visiting researcher. Furthermore, he has presented his research at the 56th, 57th, 58th, and 59th Annual AAPM conventions, the 2016 SEAAPM Symposium and Scientific Meeting, the spring 2017 Cancer Research Conference at the University of Tennessee Health Science Center, and the 3rd Annual West Cancer Center in Memphis Tennessee. In addition, he has two articles currently in progress for research completed on his scintillating fiber IMRT and SBRT/SRS detectors.